University of Seville
Interuniversity Master in Nuclear Physics

MHD stability analysis of the SMall Aspect Ratio Tokamak (SMART)

Àlex Reyner Viñolas

Supervisors:
Manuel García Muñoz
Eleonora Viezzer
Jesús José Domínguez-Palacios Durán

Departamento de Física Atómica, Molecular y Nuclear
Facultad de Física
Plasma Science and Fusion Technology

Abstract

At the University of Seville, a significant leap forward is being pursued in the race towards achieving viable fusion energy. In this pursuit, the construction of the SMall Aspect Ratio Tokamak (SMART), a spherical tokamak, is currently underway. Having good confinement is essential for the proper function of a tokamak. Different operation regimes have been proposed. The advanced tokamak regime seems to be the more promising for nuclear fusion plants. The high pressures in this regime give rise to pressure driven instabilities that deteriorate the confinement and limit the operational space. A good understanding of the instabilities is key to operate the tokamak.

The objective of this master thesis is to ascertain the influence of an ideal wall on the plasma stability. To accomplish this, `CHEASE` and `MARS-F` codes have been employed. The simulations are centered on the ideal magnetohydrodynamic (MHD) scenario, neglecting plasma rotation and kinetic effects, as well as plasma resistivity and viscosity. The aim of this simplified approach is to isolate and comprehend the fundamental impacts of the wall on plasma stability. MHD instabilites in the advanced tokamak regime for low-n modes ($n = 1, ..., 6$), and the effects of the wall at varying distances, were studied. Taking advantage of SMART's capability to operate at different triangularities, a study to determine the most favorable triangularity for achieving good confinement has been conducted. The highest positive triangularities have shown better MHD stability.

Contents

1 Introduction

1.1 Nuclear fusion

Plasma, usually called the fourth state of matter, is a highly ionized gas composed of positive and negative charges, that forms when matter is so hot and energetic that atoms are separated in ions (nucleus) and electrons. Stars, like the Sun, produce tremendous amounts of energy through nuclear fusion. While on a universal scale this process may not be eternal, we can consider it as an infinite source of energy. The plasma in their core, composed of hydrogen, helium, carbon, and other heavier nuclei, is subjected to extremely high temperatures and pressures due to the intense gravitational forces. This causes the light nuclei to fuse together, forming heavier elements and liberating energy. This process is called Nucleosynthesis.

For Sun-like stars, the dominant fusion process is the proton-proton chain. Of course, we can not replicate the same processes that occur in the core of the stars here, in the Earth. With the objective of imitating the stars, the development of fusion power plants is of special interest for our future. The ultimate goal is the creation of a fusion reactor capable of achieving sustainable, clean, and virtually limitless energy generation. The most promising reaction is the deuterium-tritium[1] fusion,

$$ {}^{2}_{1}\mathrm{D} \ + \ {}^{3}_{1}\mathrm{T} \ \longrightarrow \ {}^{4}_{2}\mathrm{He} \ + \ \mathrm{n} \ + \ Q \tag{1.1} $$

produces $Q = 17.6$ MeV of energy. Although this reaction does not yield the largest release of energy, it is the most promising one in terms of the cross-sections for the achievable temperatures (Fig. 1.1). Tritium is a highly contaminating element and does not exist in large quantities on earth. However, this problem can be solved by utilizing the neutron from the fusion reaction to induce a reaction with lithium,

$$ \mathrm{n} \ + \ {}^{6}_{3}\mathrm{Li} \ \longrightarrow \ {}^{4}_{2}\mathrm{He} \ + \ {}^{3}_{1}\mathrm{T} \tag{1.2} $$

Thus, the problem of fuel acquisition is solved, as lithium is a relatively common element, and deuterium can be found in water.

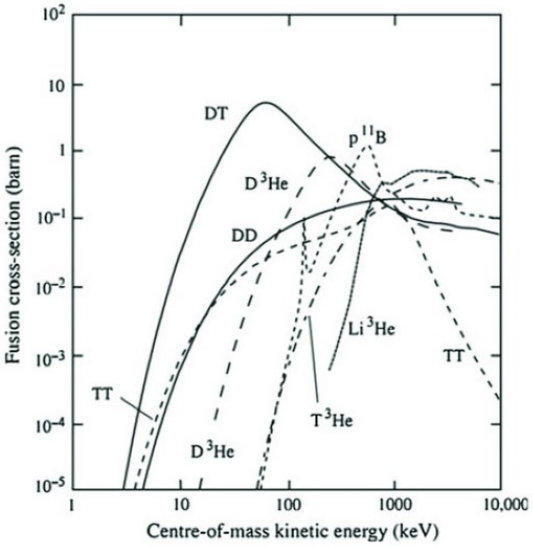

Figure 1.1: Cross sections of nuclear fusion reactions. [1]

[1] Deuterium and tritium are isotopes of hydrogen, ^{2}H and ^{3}H respectively.

1.2 The tokamak concept

As we lack the gravitational forces of the stars to confine the plasmas, we had to search other methods for plasma confinement. Since plasma is composed of charged particles, we take advantage of the Lorentz force and magnetic fields to confine the plasma. Numerous fusion devices have been designed for this purpose.

The tokamak shows the highest confinement rates so far, due to the strong decrease of MHD fluctuations at the plasma edge in the high-confinement mode (H-mode) [2]. The plasmas in tokamaks are much less denser than the ones in the stars. To compensate this and having nuclear fusion reactions we need really high temperatures ($\sim keV$). The high temperatures reached in fusion devices require avoiding physical contact with any material of the vessel, as the plasma temperature is well over the melting point of any material. In a purely toroidal confinement the toroidal component is not uniform ($B_t \propto 1/R$, being R the radius of the torus). This leads to the distinction of two regions. The high field side (HFS), located in the interior part of the torus, and low field side (LFS), in the outer most part. Therefore, a gradient directed towards the center of the torus is observed. Particles gyrating in such a non-uniform magnetic field will experience different magnetic fields during their gyration. This leads to drift forces that, eventually, will transport particles to the vessel walls. To counteract this effect, a poloidal magnetic field is added to the toroidal magnetic field. Then, the magnetic field lines take a helical shape. A schematic representation of the coils used in a tokamak, field lines, and trajectories can be seen in Fig. 1.2.

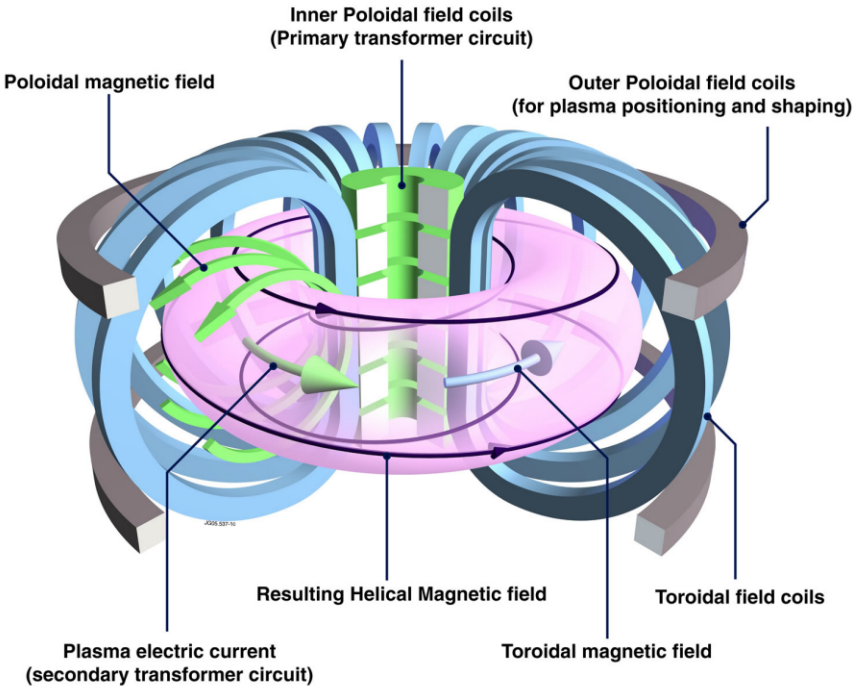

Figure 1.2: Structure of a typical tokamak device. The coils, magnetic fields and plasma are represented. Credit: EUROfusion.

In order to have profitable energy production, it is necessary for these plants to operate at a constant energy output, and be as efficient as possible and produce an equivalent or larger amount of energy. The advanced tokamak regime (AT) [3, 4] appears to be very promising for this goal. This regime is characterized by flat or reversed safety factor profiles (Fig. 1.3) and high bootstrap current, only possible for high pressures gradients. Most of the most harmful resonant surfaces are avoided due to the elevated safety factor. The normalized plasma beta [5], which is the ratio between the plasma pressure and magnetic field pressure, as it will be an important parameter in this work, is introduced:

$$\beta = \frac{2\mu_0\langle p\rangle}{\langle B^2\rangle} \quad \rightarrow \quad \beta_N = \beta(\%)(\frac{a(m)B_0(T)}{I_p(MA)}) \tag{1.3}$$

where $\langle p\rangle$ is the average plasma pressure, B_0 the magnetic field, a the minor radius and I_p the plasma current. It is especially important to control the instabilities to maximise this parameter, as fusion power scales as $\langle p\rangle^2 \sim \beta_N^2$ [6]. However, β_N is limited by numerous magnetohydrodinamic (MHD) fluctuations that deteriorate the plasma confinement and, thus, reduce the plasma β_N. The ideal external kink is the instability that limits the maximum plasma pressure achievable, which is rather low for AT tokamaks [7]. Therefore, the understanding of the physics underlying MHD instabilities, as well as of control techniques, is mandatory for future fusion reactors. The AT regime offers significant advantages only when the beta limit is significantly increased by the presence of a closely fitting wall [8].

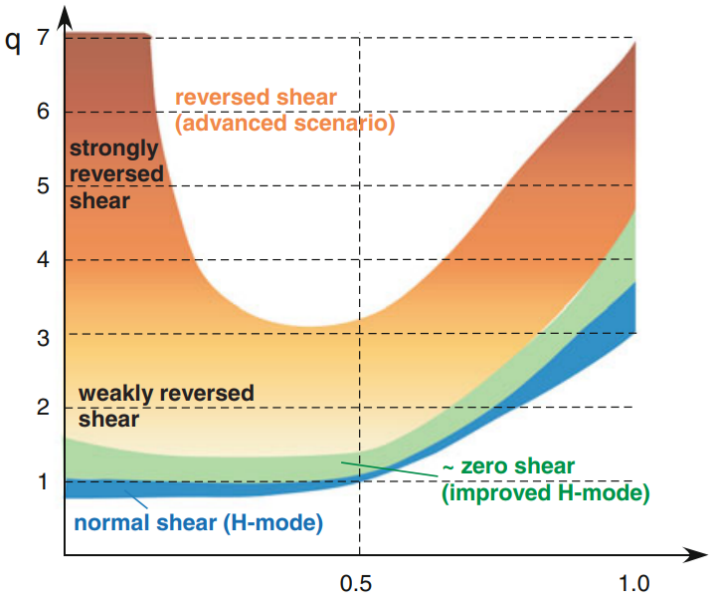

Figure 1.3: Different safety factor profiles corresponding to different scenarios. [16]

In a tokamak, the safety factor q is defined as the ratio of toroidal magnetic flux to the poloidal magnetic flux. It is expressed as,

$$q = \frac{d\Phi}{d\Psi} \tag{1.4}$$

In other words, it represents the number of toroidal turns, n, compared to poloidal turns, m, before a closed path is formed; or the helical twist of the field lines,

$$q = \frac{m}{n} \tag{1.5}$$

The safety factor gives a measure of the MHD stability of a tokamak. In general, the higher the safety factor is, the more stable it is. For a diverted tokamak [9], like the SMART, q value is mathematically infinite at the LCFS. This would imply that we always have stability for edge localized modes. However, studies have shown that this is not the case. For this type of tokamak, the q value at the 95% is often used to give a measure of the plasma stability at the edge.

Tokamaks do not have always the same size and proportions. There are conventional tokamaks and spherical tokamaks. The difference between them lies in the aspect ratio, $A = R/a$ (see Fig. 1.4). Spherical tokamaks are characterized by low aspect ratios ($A < 2$), high β, high fraction of bootstrap currents and good energy confinement. Spherical torus plasmas have large elongation, large plasma current and similar toroidal and poloidal fields. This kind of tokamak shows improved stability respect other devices. ST have more compact and simple designs, and lower cost of operation, with a fusion power similar to conventional tokamaks. [10, 11]

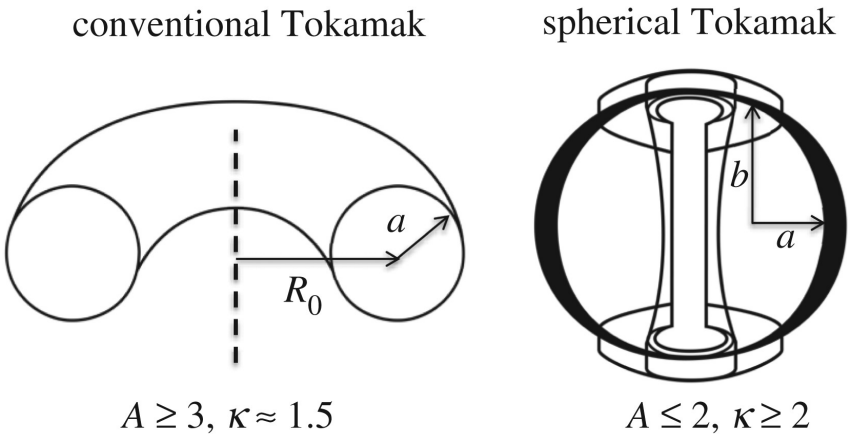

Figure 1.4: Section of a conventional tokamak and a spherical tokamak. [12]

1.3 SMART

The SMall Aspect Ratio Tokamak (SMART) [13, 14] is a new spherical tokamak being commissioned at the University of Seville. The main characteristic that differentiates SMART from other spherical tokamaks is its capability to operate in both positive triangularities (PT) and negative triangularities (NT). A cross section of the SMART can be seen in Fig. 1.5. The design of the device is very compact: the toroidal vacuum vessel has an inner and outer radius of 150 and 800 mm respectively, and 1600 mm of inner height. Two pairs of poloidal coils (PF1 and PF2) are used for plasma shaping and control. The divertor field coils (DIV1 and DIV2) are needed to achieve the desired elongation. Twelve copper coils (with four turns each one) are in charge of creating the toroidal magnetic field B_t. The plasma characteristics of the tokamak are: $R_0 \geq 0.4$ m, $a \geq 0.2$ m, $I_p \leq 500$ kA, $B_t < 1$T, pulse length of 500 ms, and neutral beam injection power of 1 MW. The main goals of the SMART are:

- Studying plasma transport and confinement in positive and negative triangularities
- Effect of shear flow velocity on edge plasma turbulence
- MHD stability and the control of energetic particle losses in high β plasmas
- Development of novel diagnostic techniques, divertor configurations, plasma facing materials and control schemes
- Formation of new generation of physicists and engineers

1.4 Structure of the work

In this work, a linear ideal MHD stability analysis of the SMART tokamak is performed. Firstly, in Sec. 2, an introduction to the magnetohydrodynamic (MHD) theory will be given, introducing the MHD and the ideal linear MHD equations. Also, main MHD instabilities analyzed in this work are described in Sec. 2.3. In Sec. 3 a brief description of the programs used in this work, `CHEASE` and `MARS-F`, and its normalization factors and equilibria definition are presented. The results of the simulations will be presented in Sec. 4. In Sec. 4.1 the results of a plasma beta scan without the inclusion of a wall. Then, in Sec. 4.2 the effects of the ideal wall on mode stability are investigated. In Sec. 4.3 a combined scan in both plasma beta and wall distance is presented. To provide more completeness to the study, a scan over several AT regimes has been conducted in Sec. 4.4. Finally, in Sec. 4.5, the effects of the plasma triangularity will be studied. Conclusions and outlook are presented in Sec. 5.

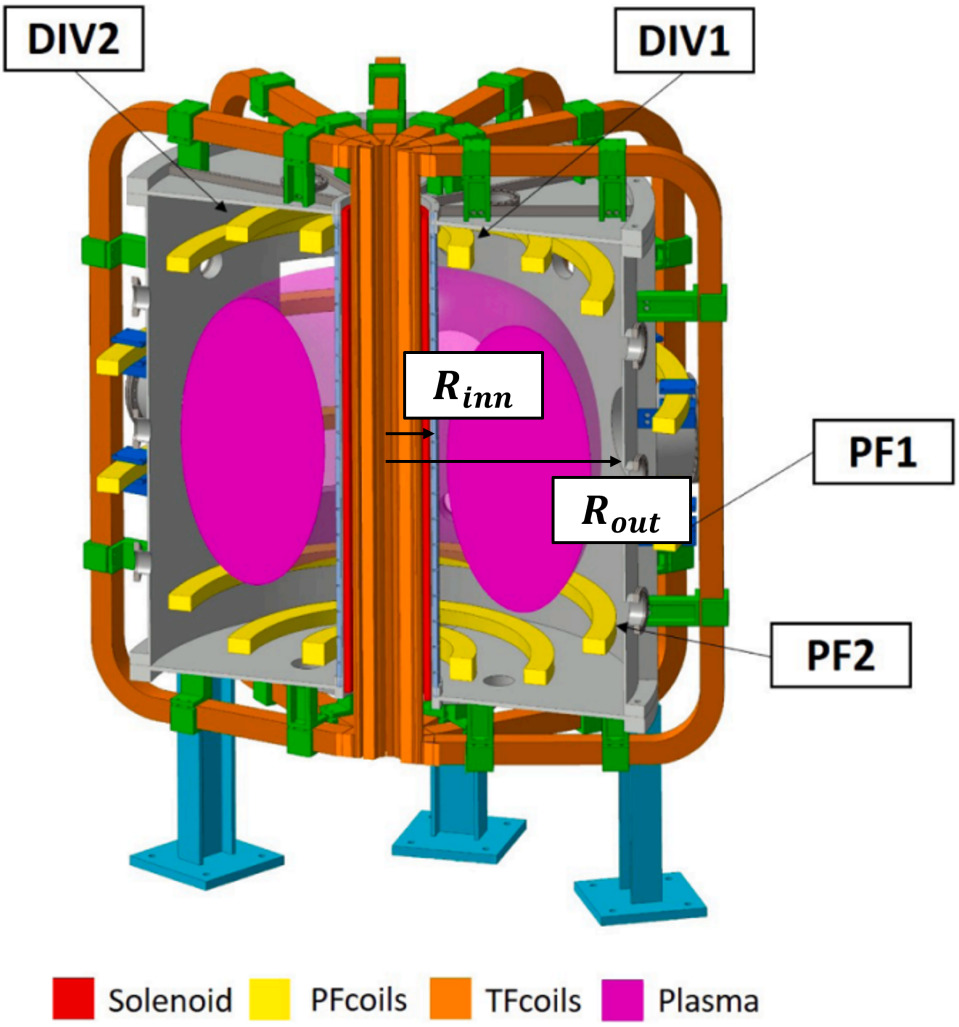

Figure 1.5: Cross section of the SMART tokamak.

2 Theoretical background

To begin with, it is necessary to grasp the concept of a plasma and the physics that governs its behavior. In this chapter, an introduction to plasmas and their fundamental characteristics will be provided. The definition of a plasma, its fundamental properties, the various descriptions used to analyze it, the confinement methods employed, and some of the instabilities observed in fusion devices are discussed in this section. For more detail, the text is based in references [15–18].

A plasma is a state of matter in which a gas becomes highly ionized, consisting of a collection of charged particles such as electrons and ions. Plasmas are known for their unique properties and behavior. They are electrically conductive, responding strongly to electric and magnetic fields. Due to the presence of charged particles, plasmas can generate and carry electrical currents. Globally, plasmas are electrically neutral when their dynamics are studied over distances larger than the Debye length. Plasmas also exhibit collective phenomena like waves with their own frequencies, instabilities, and self-organization.

Describing a plasma is not a straightforward task. Initially, one can approach the problem by considering the plasma as a collection of many individual particles and evaluating all interactions between them. This method becomes exceedingly difficult to solve as the individual behaviour of each particle in the phase space can not be described. Also, this description is not viable computationally given the elevated number of particles. Therefore, a fluid-statistic description is commonly employed to effectively deal with plasmas.

2.1 Magnetohydrodynamic model

The MHD equations describe the plasma as a charged neutral electromagnetic conducting fluid, meaning that the individual particle motion cannot be studied. The plasma is a mixture of ions and electrons. With the MHD description, both species are described by MHD equations. From them, one can obtain the one-fluid MHD equations. For this purpose, the one-fluid variables are defined below:

$$\begin{aligned} \rho &= n_e m_e + n_i m_i \approx n_i m_i = \rho_i \\ \mathbf{u} &= (n_e m_e \mathbf{u}_e + n_i m_i \mathbf{u}_i)/\rho \approx \mathbf{u}_i \\ \rho_{el} &= -e n_e + e m_i \approx 0 \\ \mathbf{j} &= -e n_e \mathbf{u}_e + e m_i \mathbf{u}_i \\ p &= p_e + p_i \end{aligned} \tag{2.1}$$

where ρ is the mass density, $\mathbf{u}$ is the velocity, ρ_{el} the charge density, $\mathbf{j}$ the current and p the pressure. The one-fluid ideal MHD continuity, momentum and energy equations, and pre-Maxwell equations form a closed set of equations (2.2),

$$\begin{aligned} \frac{\partial \rho}{\partial t} + \nabla \cdot (\rho \mathbf{u}) = 0 \qquad & \mathbf{E} + \mathbf{u} \times \mathbf{B} = 0 \\ \rho \frac{d\mathbf{u}}{dt} = \mathbf{j} \times \mathbf{B} - \nabla p \qquad & \nabla \times \mathbf{E} = -\frac{\partial \mathbf{B}}{\partial t} \\ \frac{d}{dt}(p\rho^{\gamma}) = 0 \qquad & \nabla \times \mathbf{B} = \mu_0 \mathbf{j} \end{aligned} \tag{2.2}$$

2.2 Linear ideal MHD equations

The equilibrium can be stable, unstable or metastable against small variations around the equilibrium itself. The linearization of MHD equations are a useful tool to understand the mechanisms that make the plasma unstable and, thus, develop MHD instabilities. In the following, the linear ideal MHD equations are shown. These are obtained doing a Taylor expansion of MHD variables,

$$f(\mathbf{x}, t) = f_0(\mathbf{x}) + \epsilon f_1(\mathbf{x}, t) + \mathcal{O}(\epsilon^2) \tag{2.3}$$

where $f(\mathbf{x}, t = 0) = f_0(\mathbf{x})$ and $f_1(\mathbf{x}, t = 0) = 0.$, and the ϵ parameter is small. Introducing this expansion to the MHD equations (2.2), keeping only the lineal terms, the linear ideal MHD equations are obtained,

$$\begin{aligned} \frac{\partial \rho_1}{\partial t} + \nabla \cdot (\rho_0 \mathbf{u}_1) = 0 \qquad & \mathbf{E}_1 + \mathbf{u}_1 \times \mathbf{B}_0 = 0 \\ \rho_0 \frac{d\mathbf{u}_1}{dt} = \mathbf{j}_0 \times \mathbf{B}_1 + \mathbf{j}_1 \times \mathbf{B}_0 - \nabla p_1 \qquad & \nabla \times \mathbf{E}_1 = -\frac{\partial \mathbf{B}_1}{\partial t} \\ \frac{\partial p_1}{\partial t} + \mathbf{u}_1 \cdot \nabla p + \gamma p_0 \nabla \cdot \mathbf{u}_1 = 0 \qquad & \nabla \times \mathbf{B}_0 = \mu_0 \mathbf{j}_0 \quad , \quad \nabla \times \mathbf{B}_1 = \mu_0 \mathbf{j}_1 \end{aligned} \tag{2.4}$$

The displacement vector $\boldsymbol{\xi}(\mathbf{x}, t)$ of the plasma is defined as,

$$\mathbf{u}_1 = \frac{\partial \boldsymbol{\xi}}{\partial t} \tag{2.5}$$

After introducing equation (2.5) integrating the equations (2.4), the linear ideal MHD force equation is obtained,

$$\rho_0 \frac{\partial^2 \boldsymbol{\xi}}{\partial t^2} = \boldsymbol{F} \cdot \boldsymbol{\xi} \tag{2.6}$$

where $\boldsymbol{F}$ is the linear force dyadic operator,

$$\begin{aligned} \boldsymbol{F} \cdot \boldsymbol{\xi} = \frac{1}{\mu_0} \{ & [\nabla \times \nabla \times (\boldsymbol{\xi} \times \mathbf{B}_0)] \times \mathbf{B}_0 + (\nabla \times \mathbf{B}_0) \times \nabla \times (\boldsymbol{\xi} \times \mathbf{B}_0) \} \\ & + \nabla [\nabla \cdot (p_0 \boldsymbol{\xi}) + (\gamma - 1) p_0 \nabla \cdot \boldsymbol{\xi}] \end{aligned} \tag{2.7}$$

The problem is reduced to an eigenvalue problem with,

$$\boldsymbol{\xi}(\mathbf{x}, t) = \sum_{n=-\infty}^{+\infty} \boldsymbol{\xi}_n(\mathbf{x}) \exp\{-i\omega_n t\} \tag{2.8}$$

The eigenvalues ω_n determine the stability. If $\omega_n \in \mathbb{R}$, the solution is oscillatory and the equilibrium is stable. If $\omega_n \in \mathbb{C}$, the solution grows and the equilibrium is unstable.

2.3 MHD instabilities

The plasma is a highly responsive medium, characterized by a delicate equilibrium that can be easily disturbed. Even the smallest of perturbations can trigger instabilities, turbulences, waves, etc. that change the behavior of the plasma and lead to degradation of confinement. That is why it is of utmost importance to actively prevent and carefully manage instabilities to ensure optimal control. A brief explanation of the instabilities observed in this work is given below.

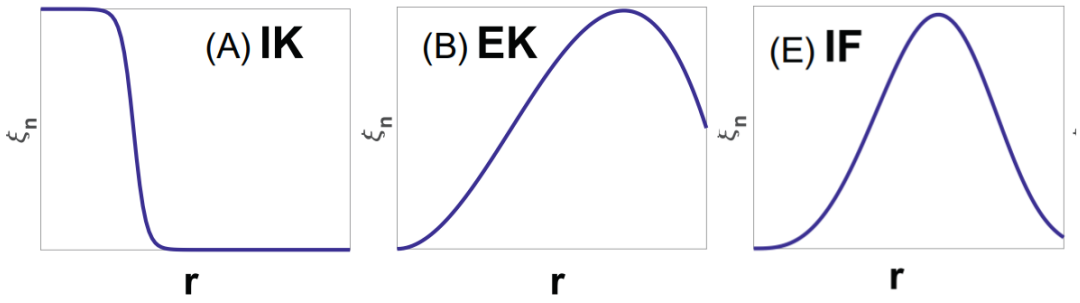

Figure 2.1: Eigenmode structure, for typical MHD instabilities: (A) internal kink, (B) external kink, (E) infernal mode. [19]

2.3.1 Internal kink

The Internal kink (IK) is an instability found in the core of the plasma. In regions where high plasma current flows, strong poloidal magnetic fields are induced by this current. If the plasma experiences a perturbation, these fields amplify it further. This kink mode consists in a shift and tilting [20] of the central plasma column without deformation, with typically $n = m = 1$. The critical condition to have an IK is to have $q_0 < 1$. This condition is, however, not sufficient for an unstable IK. In a tokamak plasma, the IK becomes unstable only if the plasma pressure exceeds certain critical value, the Bussac limit [21]. For a flat central q-profile, the ideal $m = 1$ IK may be unstable in a torus with arbitrarily small values of β. The growth rate of the IK is proportional to $(1 - q_0)$, describing a parabolic shape [22]. The presence of an IK limits the maximum current I_p achievable and the confinement, since the confinement time is proportional to I_p [17]. As will be seen in this work, even when the external kink is the dominant mode, the internal kink contribution is non negligible. The IK stability also depends on other factors, such as trapped particles, rotation and resistive effects.

2.3.2 External Kink

The External kink (EK) is a plasma current and pressure driven mode with no null edge component. The purely current driven EK becomes unstable when $q_a < m/n$ [17, 25]. This instability has a main component with a poloidal mode number m and toroidal mode number n. The most unstable case is the (2,1) mode. Thus, EK with $m/n < q_a$ are stable at negligible pressures. As usually the safety factor has high values that help

stabilize the modes caused by plasma current, EK modes induced by pressure are the most common in tokamaks. These modes typically have low toroidal mode numbers, usually $n = 1-3$. When pressure exceeds a certain threshold $\beta_{N,no-wall}$, the mode becomes highly unstable. Past this limit the EK grows really fast, with a growth rate $\gamma_0 \sim 1/\tau_A$, where τ_A is the Alfvén time. The mode becomes impossible to control and plasma confinement is lost.

However, the presence of an ideal conducting wall surrounding the plasma within a critical distance r_c has shown to have a stability effect over the EK. Below a higher β_N threshold called the "ideal-wall" limit, $\beta_{N,ideal-wall}$, the external kink is stabilized by the wall [26, 27]. This value depends on the shape and geometry of the wall, and increases the β_N limit by a factor of $1.2 - 2$. If the plasma pressure surpasses this limit, the EK will also rapidly increase like in the no-wall case.

2.3.3 Infernal Mode

The Infernal mode (IF) is a plasma current and pressure driven instability, but mainly pressure-driven. An IF is an EK with resonant surface inside the plasma, in a region where the magnetic shear is low and the pressure gradient is large around this resonant surface [17]. One of the main characteristics to identify an IF is that the main instability with (m_0,n) is coupled to the neighboring modes ($m_0 \pm 1$,n). The growth rate of the IF increases with smaller ratio between the mode and q-profile: $\delta q = q_{min} - m_0/n$, and is highly dependent on the pressure [23]. The safety factors considered in AT regime are most unstable to IF. IF is most unstable for q_{min} just below a rational number [24].

3 CHEASE and MARS-F

The `MARS-F` code [28–30] solves the standard, linearized, ideal or resistive, MHD equations (2.4) in a toroidal geometry as an eigenvalue problem. The equilibrium input to `MARS-F` is produced with `CHEASE` [31]. `CHEASE` solves the Grad-Shafranov equation for a toroidal MHD equilibria.

$$\nabla \cdot \frac{1}{R_0^2}\nabla\psi = \frac{j_\phi}{R_0} = -p'(\psi) - \frac{1}{R_0^2}TT'(\psi) \tag{3.1}$$

where j_ϕ is the toroidal plasma current density, p' the plasma pressure gradient and T is the poloidal current flux function. To solve the equation, the free functions $p'(\psi)$ and $TT'(\psi)$ need to be determined. The coordinate system used is the flux coordinate system (s, χ, ϕ), where the radial coordinate is defined as

$$s = \sqrt{\frac{\psi - \psi_{axis}}{\psi_{edge} - \psi_{axis}}} = \sqrt{\psi_N} \equiv \rho_{pol} \tag{3.2}$$

where ψ is the poloidal magnetic flux. χ is a generalized poloidal angle, and ϕ is the toroidal angle. Some important parameters mentioned in further explanations, for `CHEASE` are:

- R0: normalisation factor for the length.
- B0: normalisation for the magnetic field.
- CFBAL: scaling factor of the pressure gradient.
- $\mathrm{NV_C}$: radial resolution of final vacuum mesh, in terms of s.
- REXT: vacuum radius normalized by the minor radius of the plasma, a.

and for `MARS-F` are:

- $\mathrm{NV_M}$: cell number specifying vacuum extension.
- M1 & M2: denotes the lower and higher poloidal modes simulated.
- NWALL: number of resistive walls considered in the simulation.

The complete set of parameters and their explanations can be found in reference [32]. In `MARS-F` simulations without a wall are not possible. In our code, the boundary of the computational domain acts as an ideal conductive wall. However, if the boundary is far enough, it can be treated as if there were no wall, and the effect will be the same as an infinite vacuum. This will be seen in the next sections. The parameters values for the simulations are:

`CHEASE`: $\mathrm{NV_C}$=160, NVEXP=0, REXT=3, R0= 0.526 m, B0=0.37 T
`MARSF`: $\mathrm{NV_M}$=160, NWALL=0, M1=-9, M2=30

3.1 Equilibria definition

Equilibria with a reversed, or nearly reversed, q-profile according to the advanced tokamak regime, with $q_{min} > 1$, have been produced. Due to the way the version used of the `CHEASE` code functions q-profiles can not be entered as an input. A discretization of the pressure (RPPF), the current profile (RFUN) and the plasma boundary, or last closed flux surface (LCFS) are used to determine the equilibrium. The starting point is an equilibrium generated by the `FIESTA` code. Modifications to the current profile and plasma shape have been made to alter the output of the q-profile.

The pressure gradient is given by,

$$\text{RPPF} = 1.54\rho_{pol}^2 - 5.38 \times 10^{-8}\rho_{pol} - 1.54 \tag{3.3}$$

Instead of the TT' quantity of equation (3.1), the surface averaged current profile has been used,

$$I_{\parallel} = \frac{\oint \mathbf{J} \cdot \mathbf{B} J d\chi}{\oint \mathbf{B} \cdot \nabla\phi J d\chi} \tag{3.4}$$

The procedure followed was manually creating current profiles using analytical expressions, such as Gaussian and Fermi like distributions, as a basis.

$$G(A, x, \mu, \sigma) = A \cdot e^{-(x-\mu)^2/\sigma} \quad ; \quad F(x, \mu, \sigma) = \frac{1}{1 + e^{(x-\mu)/\sigma}} \tag{3.5}$$

Combining this expressions, current densities and q-profiles similar to those used in Refs [7, 24, 36] are obtained. Once the shape of the profile is determined, it is normalized so that its maximum value is 1. Then, to adjust the current profile amplitude a multiplier, M, is used.

$$\text{RFUN} = M \cdot \left(\frac{[G(A, \rho_{pol}, \mu, 0.2) + F(\rho_{pol}, 0.9, 0.15)] \cdot F(\rho_{pol}, 0.85, 0.05)}{([G(A, \rho_{pol}, \mu, 0.2) + F(\rho_{pol}, 0.9, 0.15)] \cdot F(\rho_{pol}, 0.85, 0.05))_{max}} \right) \tag{3.6}$$

The LCFS used is given by following expression:

$$R = R_0 + a\cos(\theta + \delta \sin\theta) \quad ; \quad Z = a\kappa \sin\theta \tag{3.7}$$

where R_0 and a are the major and minor radius respectively, κ is the elongation and δ the triangularity of the plasma. The wall used in this study will have a shape conformal to the LCFS shape, meaning it is described by:

$$R = R_0 + a_w\cos(\theta + \delta \sin\theta) \quad ; \quad Z = a_w\kappa \sin\theta \tag{3.8}$$

where a_w is the wall radius. A section of the plasma surface and wall, the surface averaged current profile, and plasma pressure gradient can be seen in Fig. 3.1.

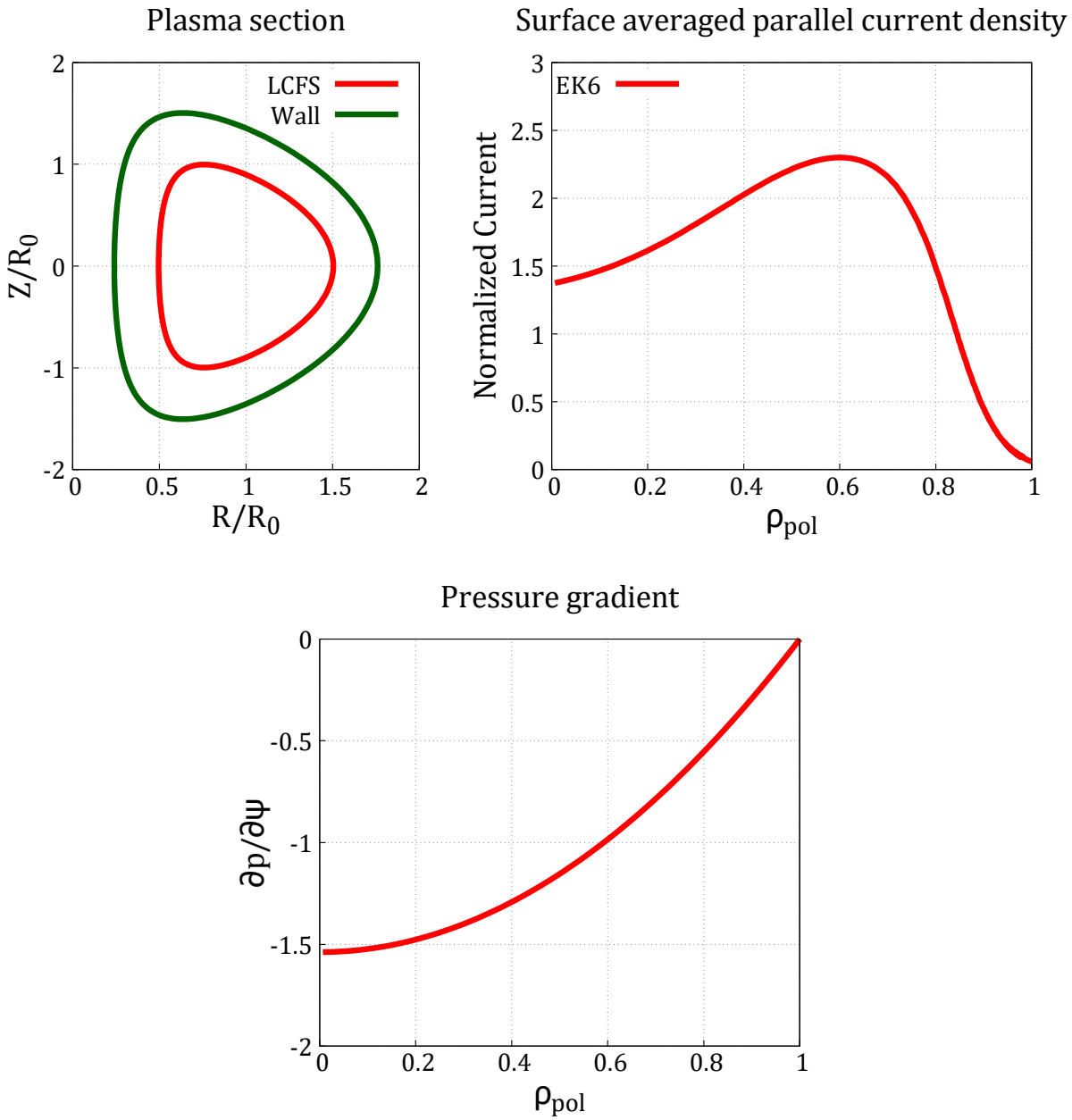

Figure 3.1: On the left, a representation of the normalized plasma LCFS and wall. In this case $R_0 = 0.53$ m, $a = 0.27$ m, $\kappa = 1.98$, $\delta = 0.5$ and $a_w = 0.4$ m. On the right, the surface averaged current profile. Below them, the ∇p input.

As mentioned, `CHEASE` produces the equilibrium input for `MARS-F` simulations from these expressions. The main characteristics of the equilibrium: total current, q-profile, plasma beta, etc.; are obtained with `CHEASE`. A problem encountered in our simulations is that `CHEASE` can not produce an equilibrium for every set of parameters, especially the high pressure equilibria ($\beta_N > 6$). Once the `CHEASE` simulation is done and the output equilibrium is produced, `MARS-F` is used to simulate the plasma stability. Among all the results obtained with `MARS-F`, the focus will be placed on the growth rate of the specific

toroidal mode n, and its mode structure. Since `MARS-F` solves the problem iteratively starting from an initial guess of the growth rate, it is possible that for some cases (mainly the most stable plasmas with lower growth rates) non-physical results are obtained. These types of results are characterized by having very narrow and tall peaks in the eigenstate structure (Fig. 3.2).

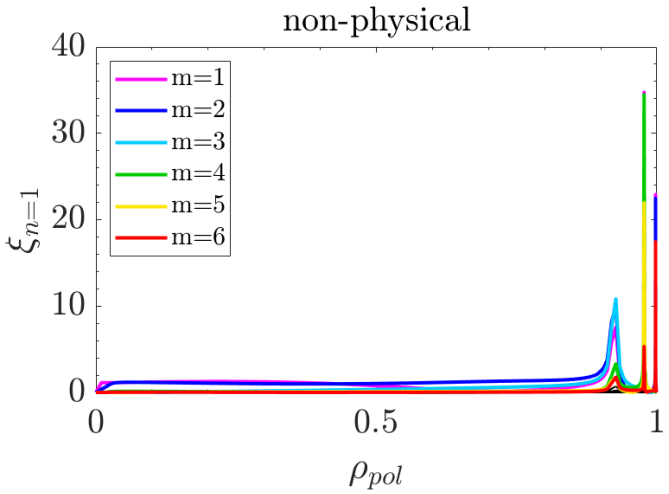

Figure 3.2: Example of a result considered non-physical.

3.2 Normalization

In this work, the normalized variables for the quantities computed are used. Table 3.1 lists the normalization used for each variable, the normalization used for each variable can be seen. Both `CHEASE` and the `MARS-*` codes share the same normalization scheme.

Quantity	SI unit	Norm. factor
length	m	R_0
mag. field	T	B_0
current	A	$R_0 B_0/\mu_0$
current density	A/m^2	$B_0/(\mu_0 R_0)$
pressure	Pa	B_0^2/μ_o
γ_0	s	ω_A

Table 3.1: Normalization factors of variables.

The Alfvén frequency, ω_A, is computed as,

$$\omega_A = \nu_a/R_0 \quad ; \quad \nu_A = B_0/\sqrt{\mu_0 m_H n_0} \tag{3.9}$$

where m_H is the Hydrogen mass and n_0 the plasma density at the magnetic axis. In this work, where $B_0 = 0.4$ T and $n_0 = 3.72 \cdot 10^{19}$ m^{-3}, the Alfvén frequency is $\omega_A = 2.514$ μs^{-1}.

4 Simulation results

Our work has been divided into four phases. Firstly, with a fixed current profile, how the increase in pressure affects our plasma has been examined. Secondly, how the ideal wall affects plasma stability. Then, a scan for different currents has been conducted. Finally, the triangularity of the plasma has been modified to produce a scan over positive and negative triangularities, using the current profile from the first part of the work. In this section the results obtained in the simulations over the different scans are presented.

4.1 Plasma β scan

For this first part of the work, the averaged current profile (3.6) is fixed to:

$$\text{RFUN}(M = 2.3,\ \mu = 0.7,\ A = 1) \tag{4.1}$$

By changing the CFBAL parameter, the pressure gradient is modified and, thus, the plasma beta is modified. Tab. 4.1 shows the different parameters of the equilibria for each CFBAL value considered. A wide range of pressures has been covered to observe the effect plasma beta has on the GR of the modes.

Tag	CFBAL	q_0	q_{min}	q_{95}	q_{edge}	β (%)	I_p (kA)	β_N
ek6v4.0	4.0	1.80	1.62	4.12	5.70	19.22	359.36	5.276
ek6v3.8	3.8	1.78	1.59	4.04	5.62	18.66	356.99	5.157
ek6v3.6	3.6	1.76	1.56	3.97	5.53	18.08	354.56	5.030
ek6v3.4	3.4	1.74	1.53	3.89	5.45	17.47	352.06	4.895
ek6v3.2	3.2	1.72	1.50	3.82	5.36	16.82	349.49	4.750
ek6v3.0	3.0	1.70	1.48	3.74	5.27	16.15	346.86	4.594
ek6v2.8	2.8	1.69	1.45	3.67	5.18	15.44	344.16	4.426
ek6v2.6	2.6	1.67	1.43	3.59	5.08	14.69	341.39	4.246
ek6v2.4	2.4	1.66	1.40	3.52	4.99	13.90	338.54	4.051
ek6v2.2	2.2	1.65	1.38	3.44	4.89	13.06	335.63	3.840
ek6v2.0	2.0	1.65	1.36	3.37	4.79	12.18	332.64	3.612
ek6v1.8	1.8	1.64	1.33	3.29	4.70	11.24	329.58	3.364
ek6v1.6	1.6	1.64	1.31	3.22	4.59	10.24	326.45	3.096
ek6v1.4	1.4	1.64	1.29	3.14	4.49	9.19	323.25	2.805
ek6v1.2	1.2	1.65	1.28	3.07	4.39	8.07	319.99	2.488
ek6v1.0	1.0	1.65	1.26	2.99	4.29	6.89	316.68	2.146

Table 4.1: q_0, q_{min}, q_{edge}, plasma beta, total plasma current and normalized plasma beta (1.3) for different CFBAL values. The tag allows us to reference each case.

Fig. 4.1 illustrates the pressure and safety factor profiles for some of the cases listed in Tab.4.1. This equilibrium returns us a slightly reversed q-profile, with a q value at the edge close to 5. This is a typical profile for an AT scenario (see Fig. 1.3). Since `CHEASE` calculates the equilibrium for each CFBAL value self-consistently, this implies that not all the equilibirum parameters can be kept constant when changing one of them (in this case,

CFBAL). It can be observed that q decreases with decreasing pressure. When changing the pressure is expected to have a slight change in the q-profile, specially in the edge zone. In our case this change is more global. From Tab. 4.1, it can be seen that q_{edge} changes $\sim 28\%$, $q_{95} \sim 32\%$, $q_{min} \sim 25\%$ and $q_0 \sim 10\%$. The effects of a change like this can modify the results obtained for the GRs. There is also an important value change on the total current I_p, that varies $\sim 10\%$.

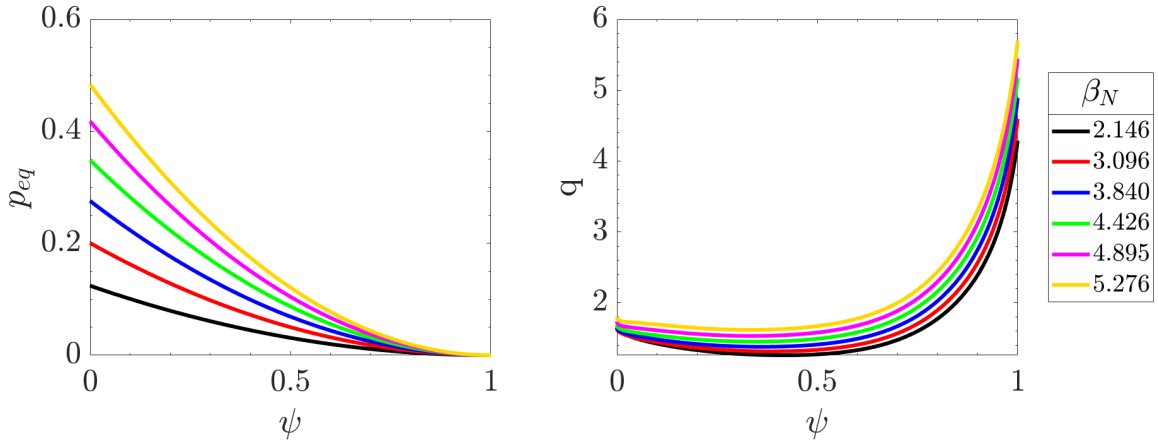

Figure 4.1: Pressure and safety factor for some of the EK6 equilibria.

The growth rates and eigenfunctions for modes $n = 1, ..., 6$ have been computed. Fig. 4.2 shows the normalized GR of these modes for some cases of the plasma beta scan. A clear tendency for an increase in the GR with plasma beta can be seen. For the lowest pressures, the GR has an oscillatory behaviour with the toroidal mode number n. For elevated pressures, this behaviour disappears and the the GR increases monotonically with n.

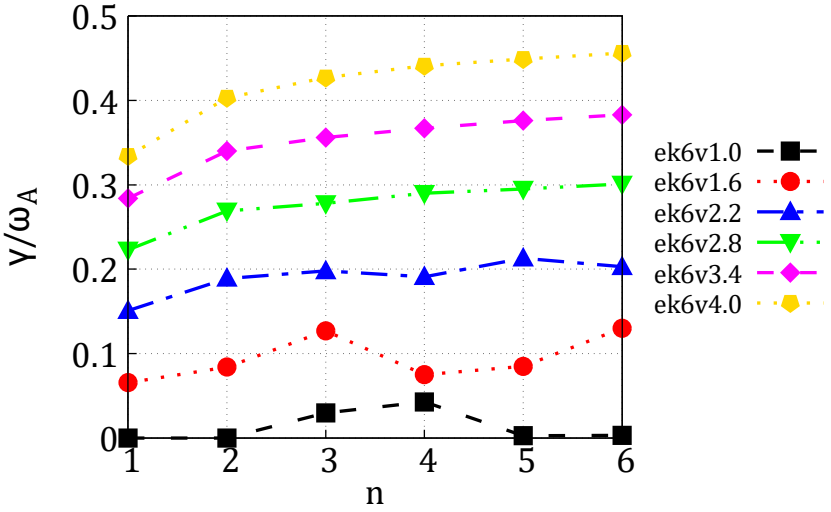

Figure 4.2: Normalized growth rates obtained for some of the simulations of the EK6 equilibria. Full data in Tab. A.1 in the appendix.

In Fig. 4.3 all the modes are plotted for the ek6v3.0 case. For $n = m = 1$, despite having $q_0 > 1$, an IK with edge component can be seen. Plasmas with this kind of q-profile are unstable for the IK even for high q_{min} and β [33]. For lower β the $n = 1$ mode is unstable for the $m = 1$, and as plasma pressure is increased the $m = 2$ contribution gains importance. The IF modes are also unstable in this regime. The GR of these IF has an oscillatory character over n, as observed in this work, that becomes stronger as q_{min} increases until a certain value where it disappears [33]. In this case, EK are mainly present in modes $n = 1, 2$ and even 3. EK can be identified by their component at the boundary, and because they are globally defined. The higher n IF are also coupled to an EK.

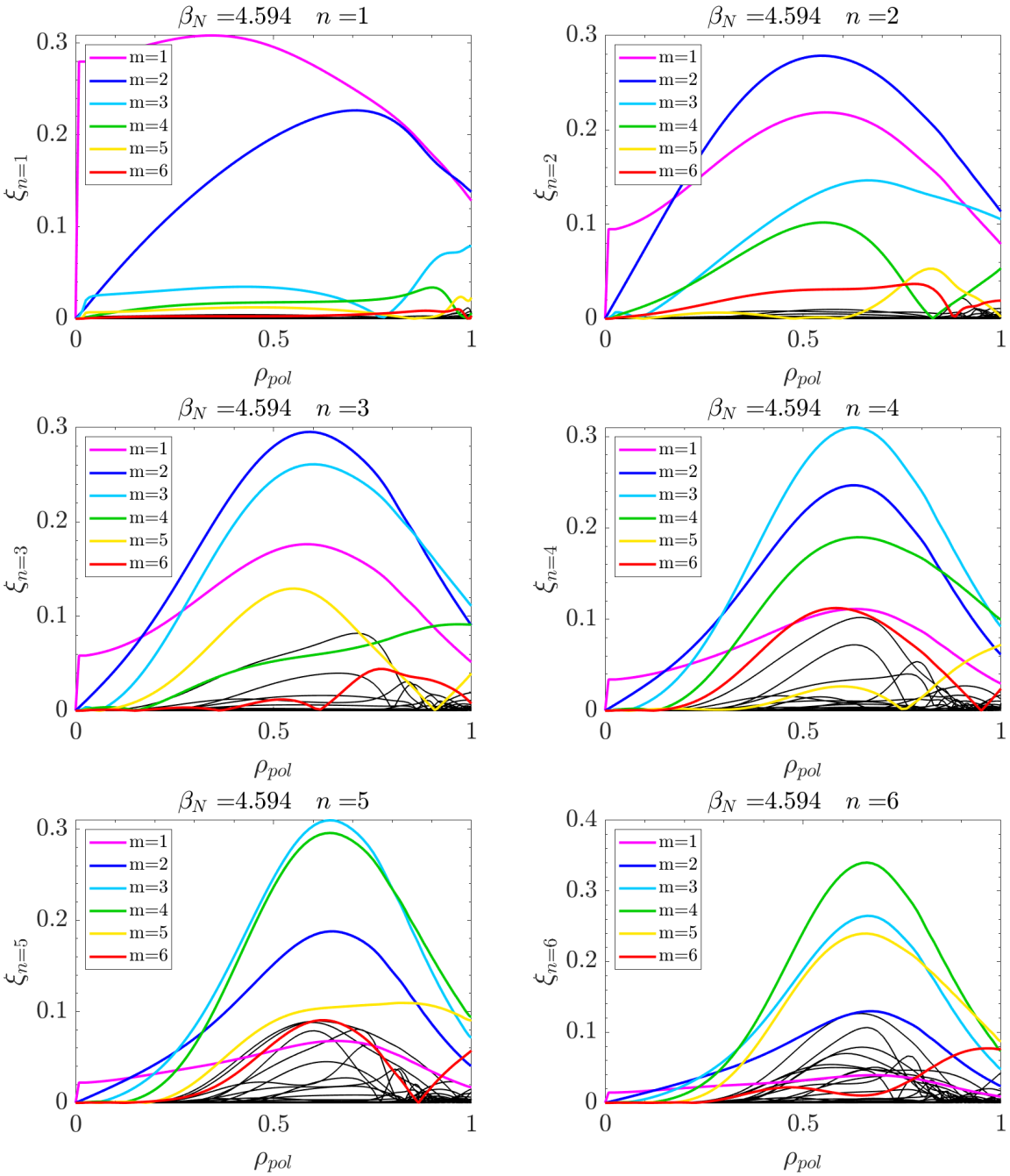

Figure 4.3: Eigenstate structure of the $n = 1, ..., 6$ modes for the ek6v3.0. The dominant poloidal modes $m = 1, ..., 6$ has been marked to differentiate them.

4.2 Ideal wall inclusion

Our goal is to study the effect that an ideal wall has on the stability of the external kinks. Tthe EK6 equilibrium with CFBAL=3 (tag: ek6v3.0, Tab. 4.1) has been choosen, because this case has a normalized plasma beta value $\beta_N = 4.6$, reasonable for the operation of a spherical tokamak [17]. This case will be named as the ICW6 equilibrium, in particular the icw6v3.0 case. The ideal wall effects are investigated changing the $\mathrm{NV_M}$ parameter in `MARS-F`, i.e., by changing the radial location of the ideal wall. By setting $\mathrm{NV_M}$=$\mathrm{NV_C}$, the entire vacuum region is included, as in the previous section. Otherwise, the ideal wall condition at the plasma boundary is achieved by setting $\mathrm{NV_M}$=1. The relation between the wall radius and $\mathrm{N_M}$ in an equidistant mesh is,

$$\frac{r_w}{a} = 1 + (\mathrm{REXT} - 1)\frac{\mathrm{NV_M} - 1}{\mathrm{NV_C}} \tag{4.2}$$

Fig. 4.4 shows the normalized linear GRof $n = 1, ..., 6$ modes for different ideal wall radial locations. For low n values, the component at the edge has more influence on the mode's GR, making the effect of the wall more pronounced. As n increases, the effect appears for shorter distances of the ideal wall respect of the LFCS. This suggests that for these n values, the dominant IF is not stabilized by the wall. If the wall very close enough to the plasma, these modes are partially stabilized as well.

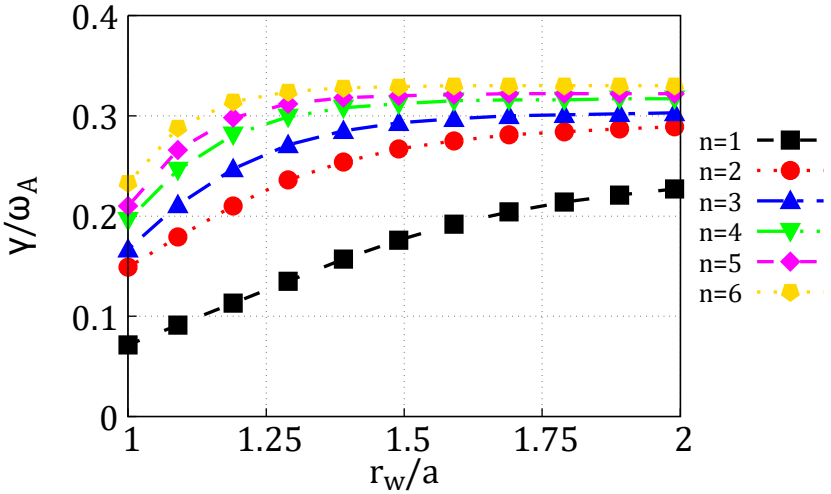

Figure 4.4: Normalized growth rates versus the ideal wall radius. Modes with lower n are affected by the wall effect earlier. Data in Tab. A.2 in the appendix.

The results obtained for the case with the closest wall are shown in Fig. 4.5. It is worth noting that while the outermost component becomes negligible in all cases, the modes still exhibit their IK and IF with the same dominant poloidal number. Having a wall prevents the displacement from expanding to the plasma edge. In Fig. 4.6, the evolution of the $n = 1$ in terms of the wall distance can be seen. The IK is not suppressed in any case and its contribution to the GR is really important. The internal component of the modes is barely affected by the ideal wall presence, and is probably the reason why the GR tending to zero at a certain radius is not observed, r_c, as seen in the literature [34, 35].

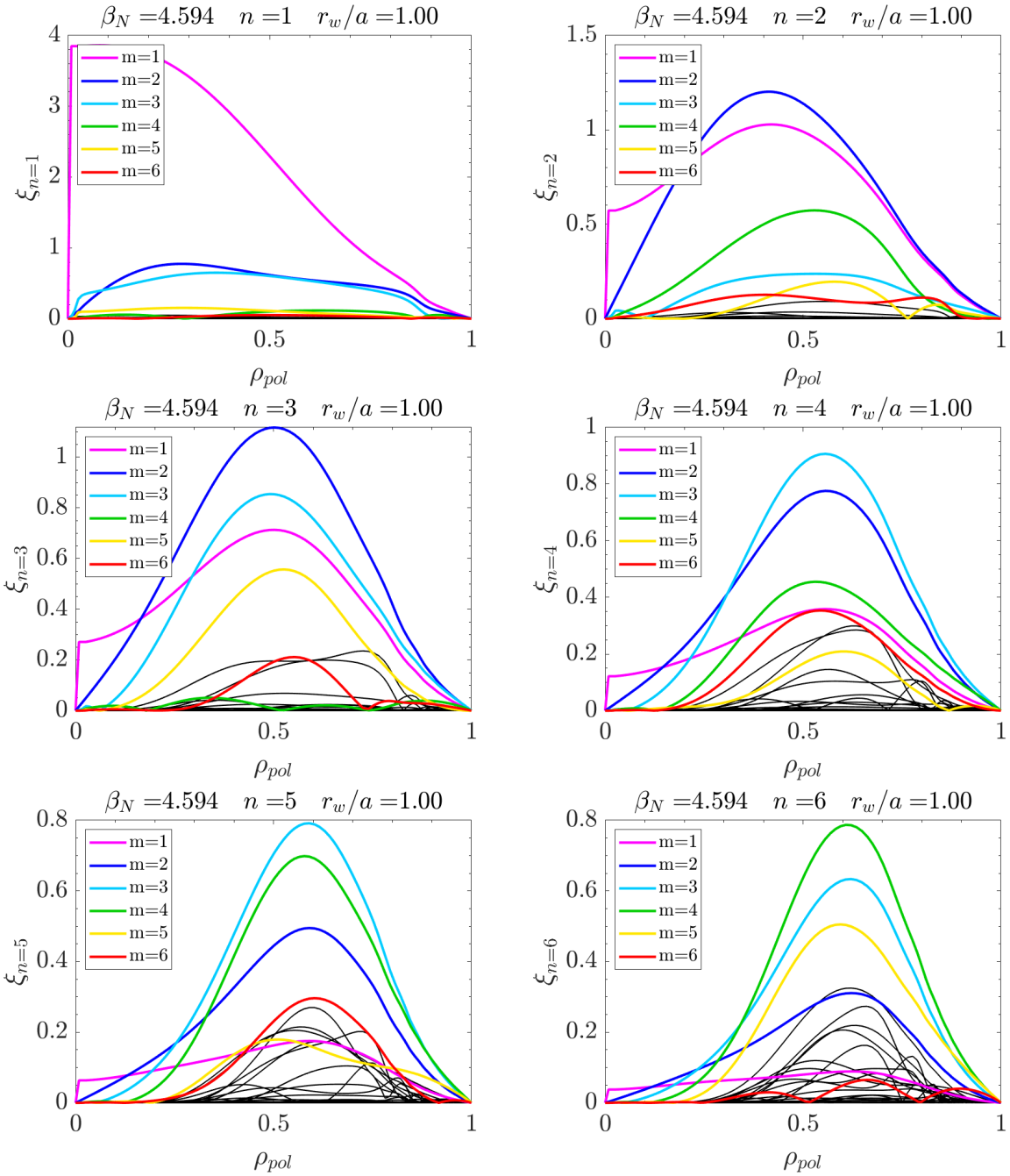

Figure 4.5: Eigenstate structure of the $n = 1, ..., 6$ modes for the icw6v3.0 with the wall at the LCFS. The dominant modes $m = 1, ..., 6$ has been marked to differentiate them.

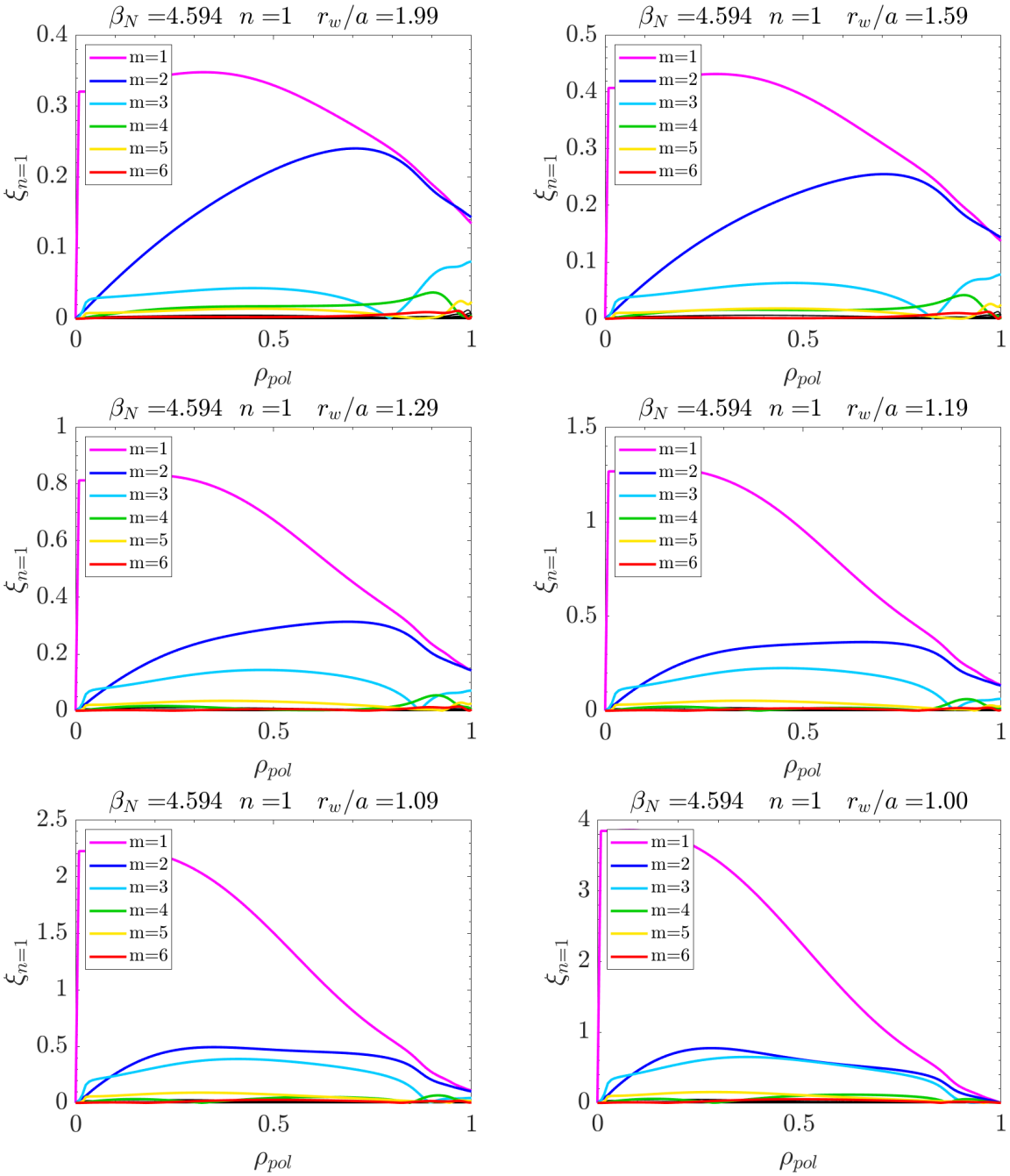

Figure 4.6: Evolution of the eigenstate structure of the $n = 1$ mode for different wall radius. The dominant poloidal modes $m = 1, ..., 6$ has been marked to differentiate them.

4.3 Plasma β and wall distance scan

So far, how the wall affects the various toroidal modes n for an specific β_N has been studied. The equilibrium studied is not stable for this pressure even with the ideal wall inclusion. For a more comprehensive study, it is necessary to determine the pressures and wall distances for which the plasma is stable. For this purpose, special focus has been put on the modes $n = 1$ and $n = 2$. Fig. 4.7 shows the linear GRof $n = 1$ and 2 modes as a function of normalized beta and wall radius. It can be observed that, indeed, the GR of the two modes increases as normalized plasma beta rises for any fixed wall distance.

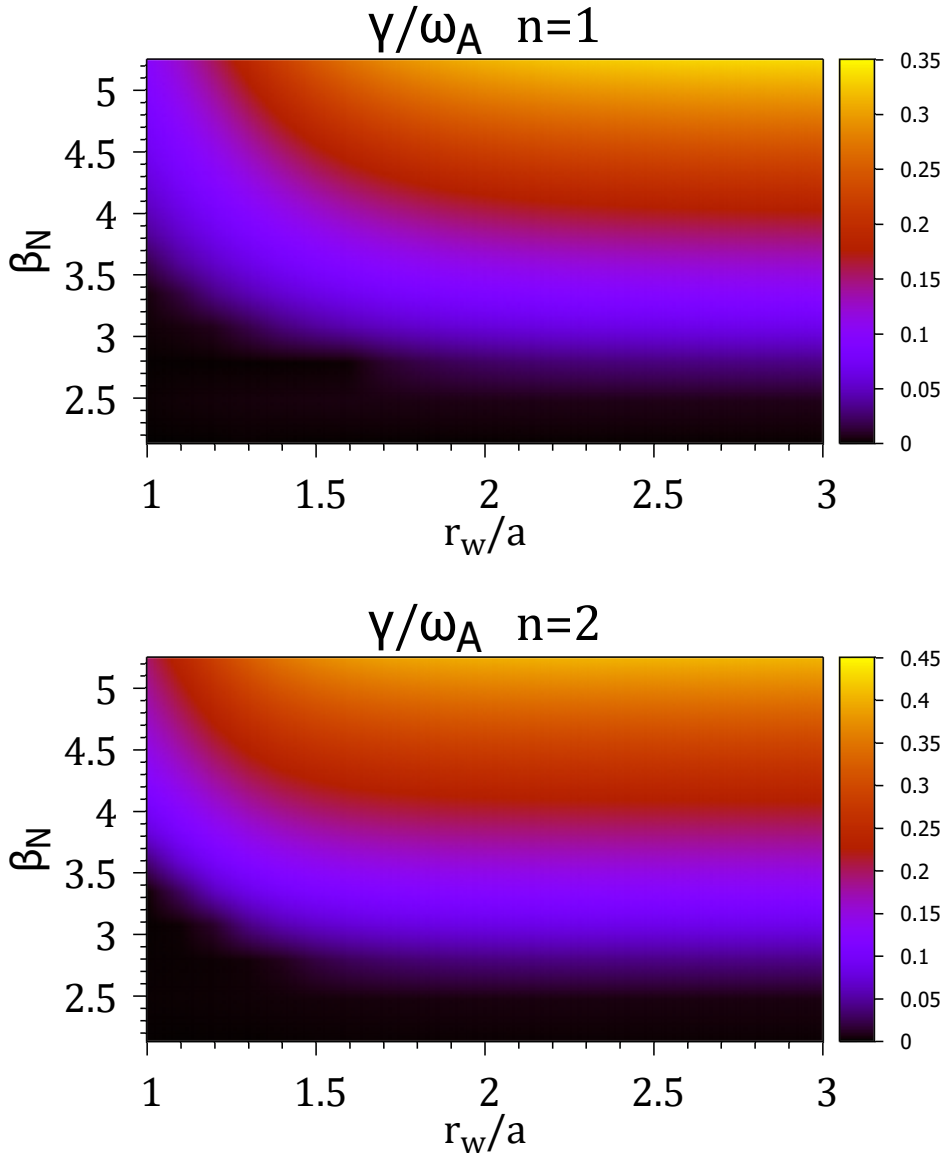

Figure 4.7: Normalized growth rates for the $n = 1$ and $n = 2$, as a function of plasma beta and wall radius. Data interpolated from a 21x16 simulation mesh.

On the right side, there is a region where the values of the GR do not vary with the

wall. This is because at that distance, the effects of the wall are not noticeable. Hence, our assumption of considering $r_w = 3$ as the case without a wall (infinite vacuum) made in Sec. 3 and used in the previous sections is indeed correct. For both cases, a lower GR region can be seen on the left side, corresponding to the stabilization of the EK by the ideal wall. For $n = 1$, the effect of the wall starts to be noticeable at $r_w/a \approx 2$. For $n = 2$, the effect of the wall starts to be noticeable at $r_w/a \approx 1.5$. Therefore, the stabilization is more effective for $n = 1$.

In Fig. 4.8 the GR of the $n = 1$ and $n = 2$ for the "no-wall" and $r_w/a = 1.00$ cases are plotted. From these results, an approximation of the β_N limits can be obtained by extrapolating when the GR becomes zero. Since the linear approximation did not yield good results, the order of the approximation has been increased by one. Also, IF modes GR is proportional to β^2, and the results show a high presence of them. Higher orders provide better results for fitting, but second-order polynomial is sufficient.

$$\gamma_0 = c_2 \cdot \beta_N^2 + c_1 \cdot \beta_N + c_0 \tag{4.3}$$

The lowest pressure points have not been used in obtaining the polynomial fit. They diverged from the behaviour of the highest pressure results and the eigenstate structure of the modes is different. The β_N limits obtained are almost the same for the two cases. Thus, it can be concluded that for this case $\beta_{N,no-wall} \approx 2.4$ and $\beta_{N,ideal-wall} \approx 3.3$, which represents an increase of approximately 37%, close to the typical 40% increase observed for ideal walls [36].

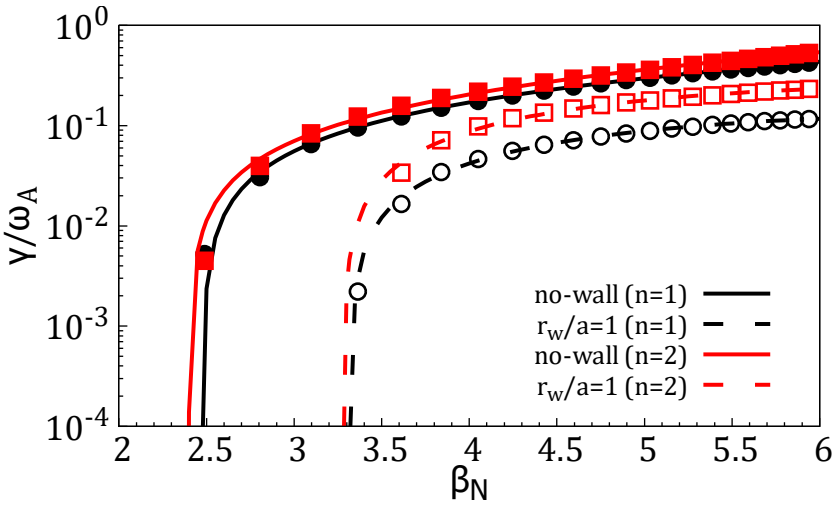

Figure 4.8: Normalized GR of the $n = 1$ and $n = 2$ modes vs β_N, for the "no-wall" case and ideal wall at the LCFS. The second-degree polynomial approximated to the data is also plotted. Full data and approximation parameters in Tab. A.3.

As mentioned before, for low pressures the modes obtained are more diverse. The most notable case is for $\beta_N = 2.49$. For $n = 1$ (see Fig. 4.9) a peak emerges in the mode structure at a poloidal radius corresponding to the $q = 2$ surface. This peak at all r_w values but increases for $r_w/a < 2.2$. Additionally, for this same pressure, the $n = 2$ (see

Fig. 4.10) mode exhibits a structure resembling the RWM found in the literature [36]. These peaks correspond to the surfaces $q = 1, 1.5, 2, 2.5, ...$ and so on. Since it is the $n = 2$ mode, they correspond to the $m = 2, 3, 4, 5, ...$ surfaces ($m = q \cdot n$). For plasma beta above $\beta_N = 2.49$ this structures are also present, but only for the the cases where the ideal wall is really close to the LCFS. However, all these modes correspond to the region with the smallest GR and have been considered them as residual perturbations.

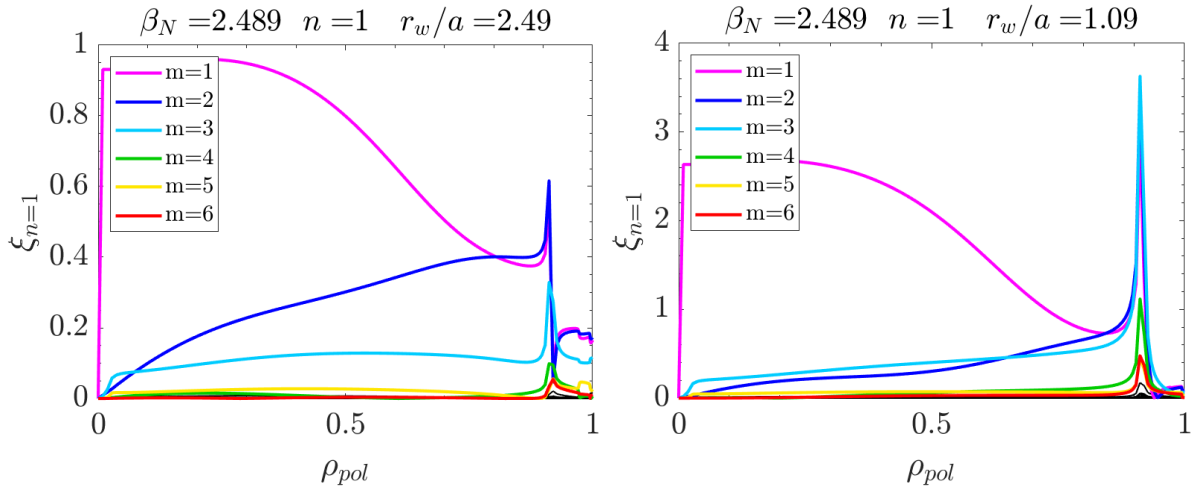

Figure 4.9: Eigenstate structure of the $n = 1$ mode at low pressure.

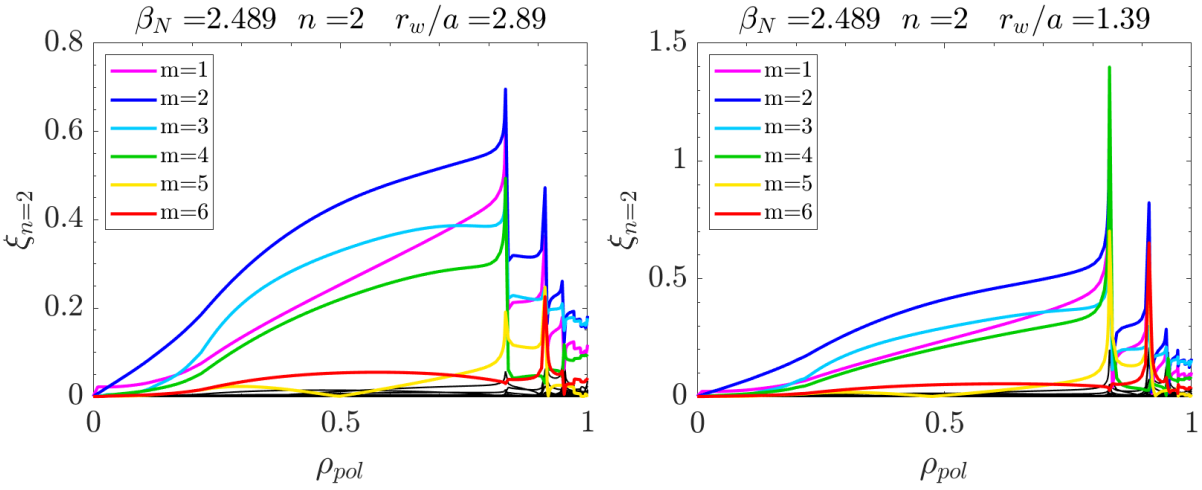

Figure 4.10: Eigenstate structure of the $n = 2$ mode at low pressure.

4.4 AT regime scan

A study for numerous regimes in SMART has been conducted, with different current profiles, to identify what equilibria are stable against IK, EK and IF. Let us recall the RFUN equation (3.6). The parameters of the Gaussian distribution are the ones changed in this scan of current profiles, while the rest is held constant. In this way, an AT scenario-like q-profile is maintained. In Fig. 4.11 it can be seen how the q-profile changes when the current is modified. Increasing the current amplitude causes an overall decrease in the entire q-profile. If central region of the current profile is fixed and the core region reduced the safety factor increases only in the core region, with a minor change in the edge. Hence a more reversed q-profile.

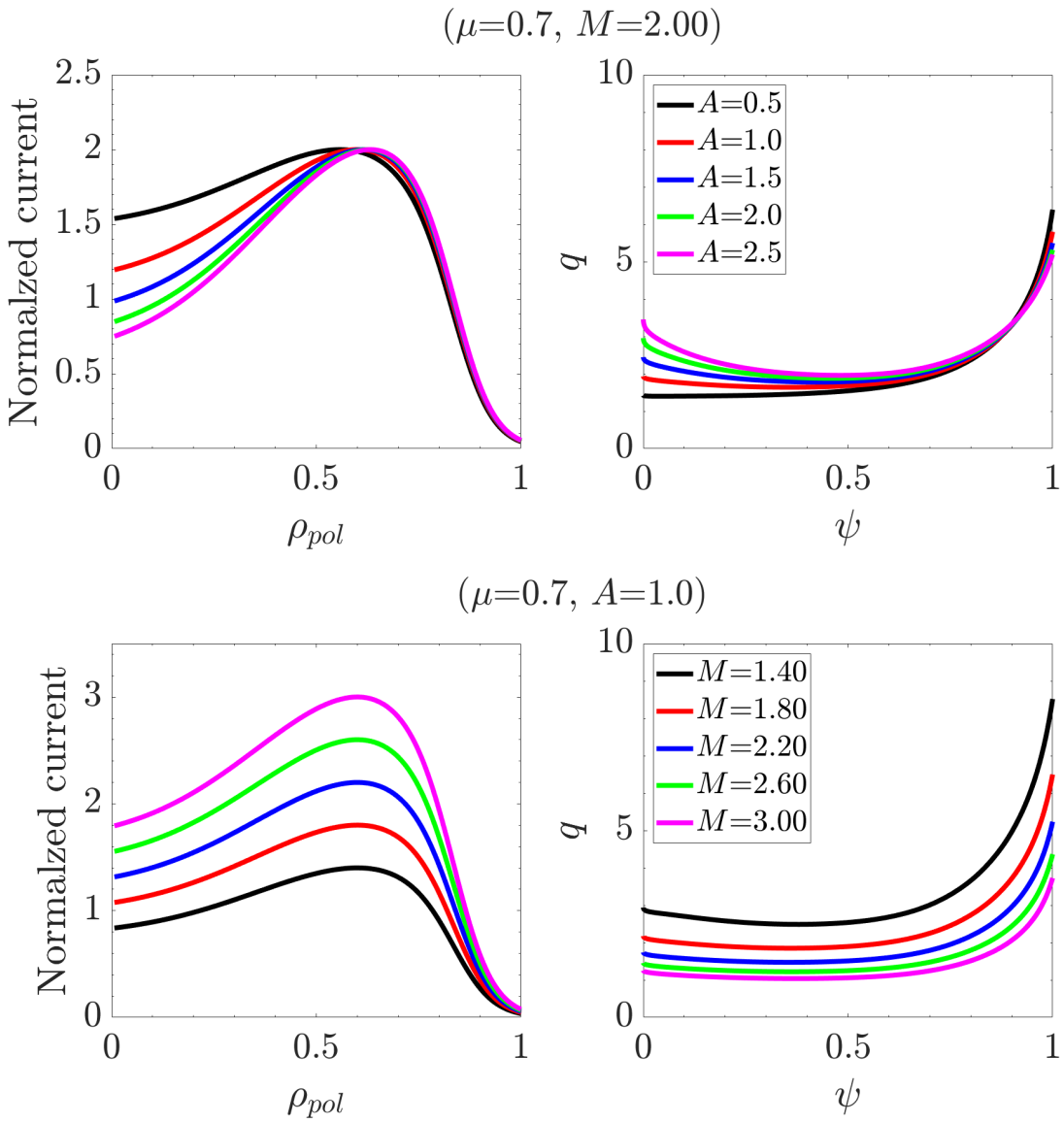

Figure 4.11: Change in the surface averaged current profile and the resulting q-profile according to the change in the RFUN parameters.

Simulations have been conducted for different current profiles with $A = 1$ and $A = 2.5$, over a broad set of pressures, for the $n = 1$ and $n = 2$ modes, with and without the ideal wall. The GR results have been filtered to determine which equilibria are stable. The GR threshold value below which the equilibrium has been considered stable is $\gamma_T/\omega_A = 1 \times 10^{-3}$. The mode profiles have been studied, and it has been found that this value is a good discriminator for ruling out where there are not IK, EK, or IF. Some simulations have converged to non-physical results (see Fig. 3.2). To identify these modes, a more in-depth study was conducted by identifying the peaks of each mode. If the width of the highest peak is lower than 0.03, the mode is considered to be non-physical, and if the value was lower than $\gamma = 5 \times 10^{-3}$, the mode has been considered stable. For cases where the current profile is very high, the q_{min} drops to values below 1. The results corresponding to this cases have been also filtered out.

Fig. 4.12 shows the results for the $A = 1$ equilibria, and Fig. 4.13 shows the results for the $A = 2.5$ equilibria. The results show that SMART exhibits stability for $\beta_N < 3$ without a wall. When an ideal wall is considered, the region of stability increases to $\beta_N \approx 6$. Similar results has been obtained in studies for other spherical tokamaks [37,38]. At high currents the stabilization thanks to the ideal wall is less effective. The β_N limit found presents a step like behaviour, found also in [39]. Comparing both figures, it can be seen that having a more reversed q-profile gives us access to higher normalized current operational range. In Fig. 4.14 the GR obtained for the RFUN($M = 1.90$, $\mu = 0.7$, $A = 1$) equilibrium are plotted. It can be seen that the β_N limits found change substantially from the ones found in Fig. 4.8. While the $\beta_{N,no-wall}$ limits for both $n = 1$ and 2 are almost the same, the $\beta_{N,ideal-wall}$ are significantly increased from $\beta_{N,ideal-wall} \approx 3.3$ to $\beta_{N,ideal-wall} \approx 5$.

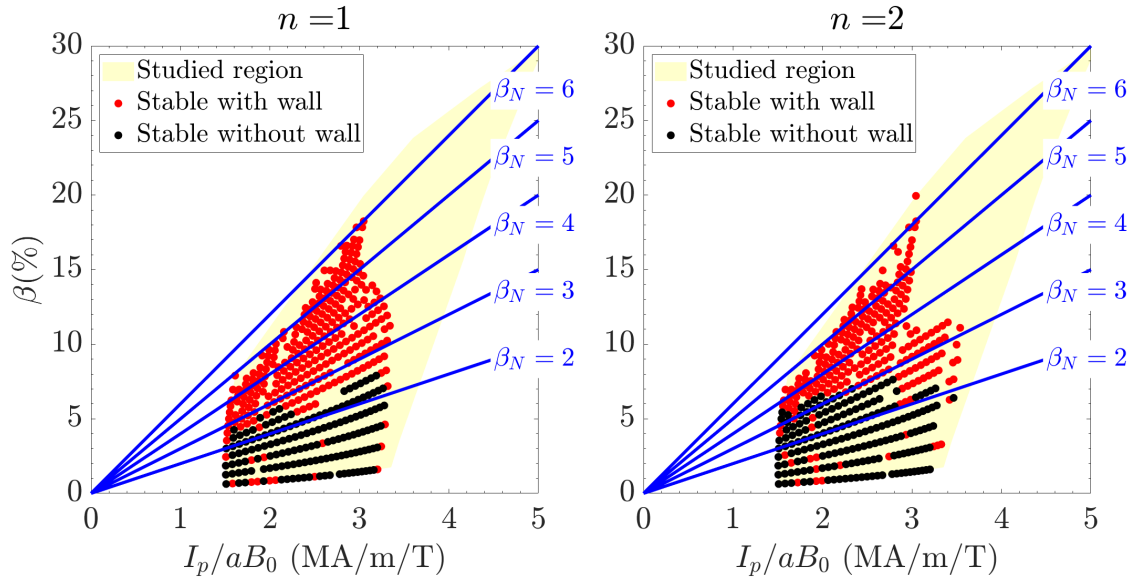

Figure 4.12: Operational range for equilibria with $A = 1$. β_N vs. normalized current for equilibria found stable without the presence of an ideal wall (black) and with an ideal wall at the LCFS (red). The parameters of the equilibria are in Tab. A.4. $B_0 = 0.4$ T.

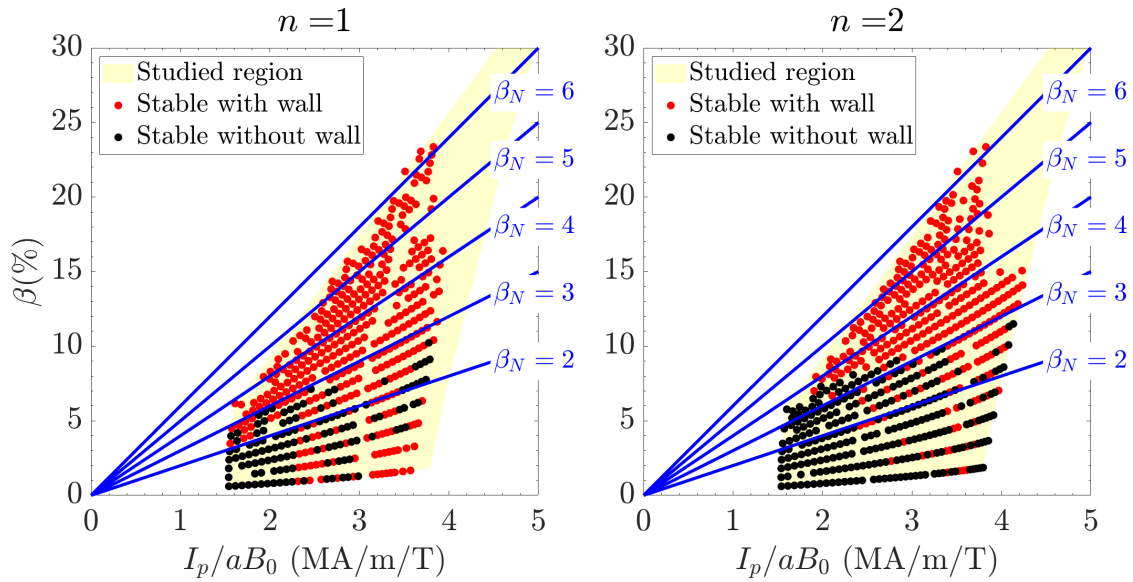

Figure 4.13: Operational range for equilibria with $A = 2.5$. β_N vs. normalized current for equilibria found stable without the presence of an ideal wall (black) and with an ideal wall at the LCFS (red). The parameters of the equilibria are in Tab. A.4. $B_0 = 0.4$ T.

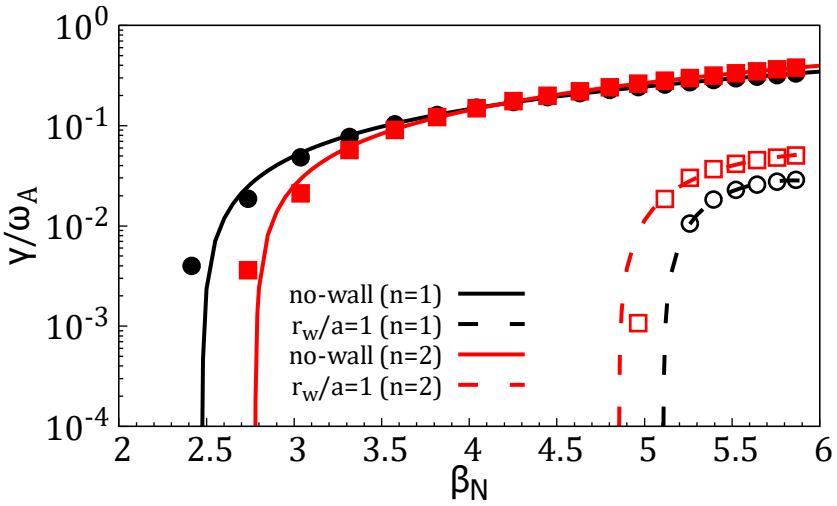

Figure 4.14: Normalized growth rates of the $n = 1$ and $n = 2$, for the "no-wall" case and ideal wall at the LCFS, vs β_N. Equilibrium: RFUN($M = 1.90,\ \mu = 0.7,\ A = 1$).

4.5 Triangularity scan

As mentioned in Sec. 1.3, SMART has been designed to operate with positive and negative triangularities. In the following, the effects of the triangularity on mode stability are discussed. Until now, the triangularity has been fixed to $\delta = 0.5$. A scan has been conducted over trinagularities between 0.3 and -0.3 (Tab. A.5). `CHEASE` has been unable to obtain the equilibrium for $\delta = -0.5$. In this scan, the pressure gradient and average parallel current density input are fixed to the EK6 equilibrium (Fig. 3.1). The shape of the LCFS and wall changes according to equation (3.7). In Fig. 4.16 it can be seen how changing δ modifies the q-profile. Due to the change in plasma shape [40], for decreasing triangularities the q-profile becomes more reversed, and the edge value is lower. The pressure profile also changes for different triangularities, but not as much as the safety factor.

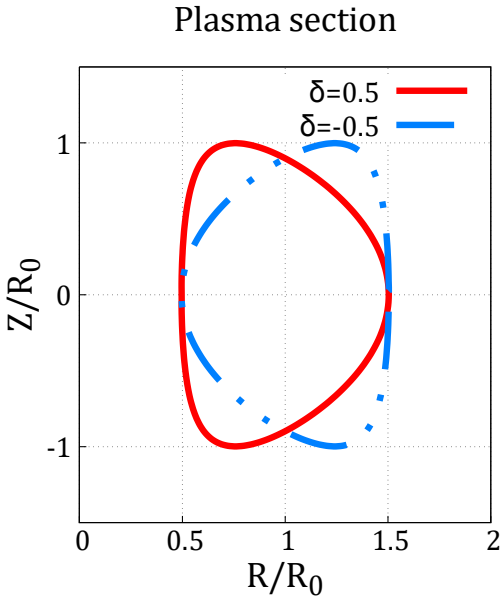

Figure 4.15: LCFS for two different triangularities.

Triang.	q_0	q_{min}	q_{95}	q_{edge}	β (%)	I_p (kA)	β_N
$\delta = 0.5$	1.70	1.48	3.74	5.27	16.15	346.86	4.569
$\delta = 0.3$	1.91	1.51	3.27	4.04	17.61	359.33	4.809
$\delta = 0.1$	2.12	1.53	2.93	3.40	18.94	366.62	5.068
$\delta = -0.1$	2.82	1.53	2.71	3.08	20.08	366.62	5.375
$\delta = -0.3$	2.92	1.54	2.64	2.98	20.55	360.21	5.600

Table 4.2: q_0, q_{min}, q_{edge}, plasma beta, total plasma current and normalized plasma beta (1.3) for different triangularity simulations.

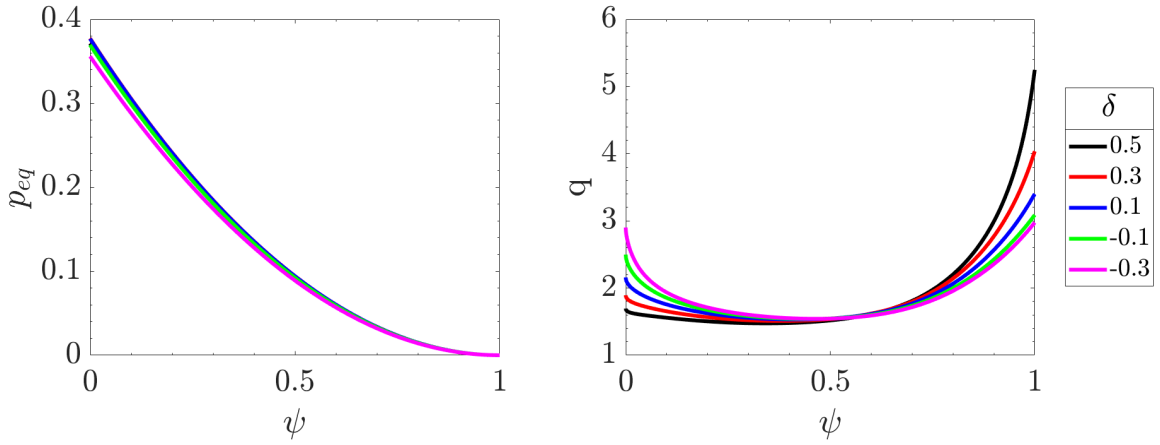

Figure 4.16: Pressure and safety factor for the different triangularities.

In Fig. 4.17 the GRs without considering the ideal wall in the simulations are presented. It can be observed that the GR increases for decreasing triangularity. This shows that for our case of study PT are better than NT. Its interesting to see that $\delta = 0.3$ gives us a lower GR than $\delta = 0.5$, except for $n = 1$.

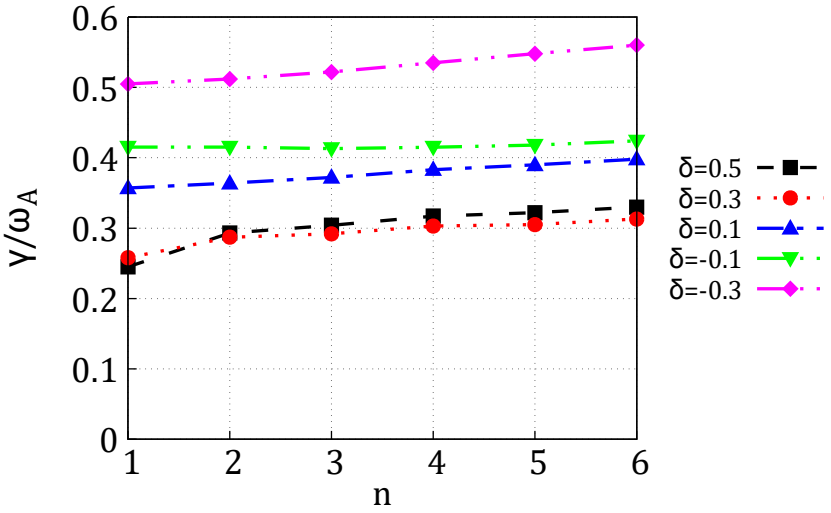

Figure 4.17: Normalized growth rates versus the toroidal mode number n, without considering an ideal wall, for different triangularities. Full data in Tab. A.5 in the appendix.

In Fig. 4.18 the GRs with an ideal wall in the simulations are presented. As expected, the wall affects the plasma stability in both PT and NT. The main difference is how the wall affects the modes. For the $n = 1$ mode, for $\delta = 0.3$, the decrease in GR is progressive with wall distance, while for $\delta = -0.3$, the effect of the wall increases significantly when it is brought close to the LCFS. This behavior leads us to think that this mode has a greater component at the edge, or that the IK is less important than for $\delta = 0.3$, since it has been observed that the effect of the wall on the IK is less noticeable than on the EK. In Fig. 4.19Ir can be see how, indeed, this mode has less edge component. This change in the profile is probably because of the change in the q-profile (higher q_0 and lower q_{edge}).

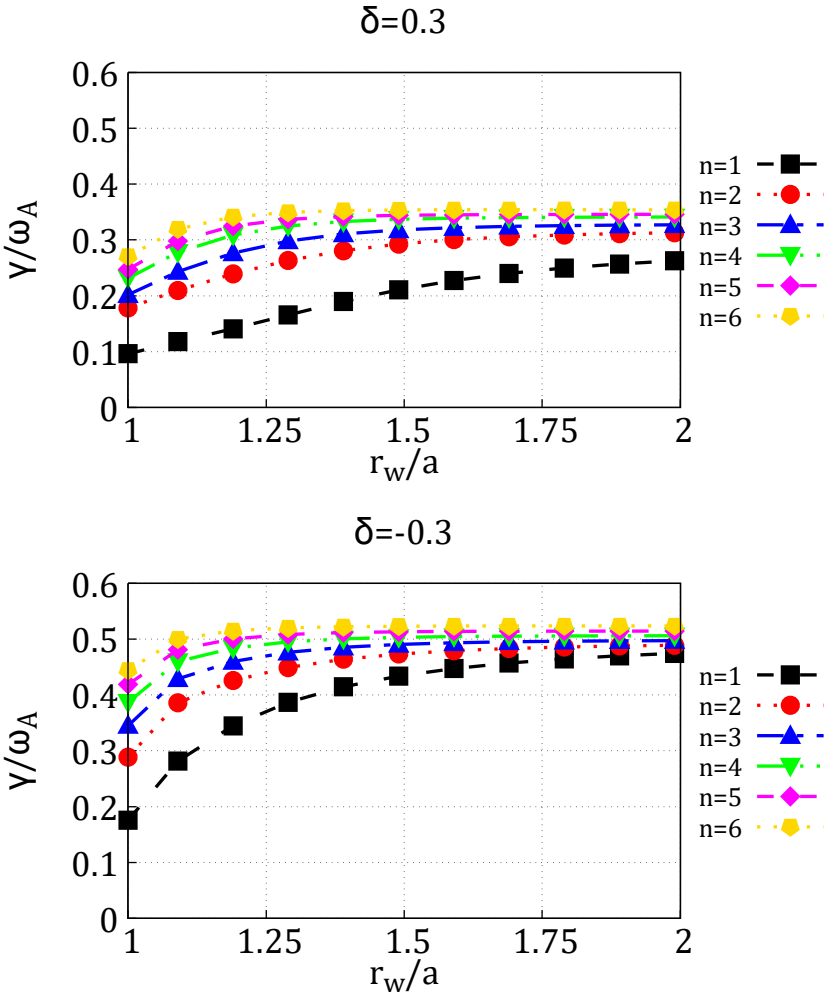

Figure 4.18: Effect of the ideal wall on the normalized growth rates of the $\delta = 0.3$ and $\delta = -0.3$ triangularities for modes $n = 1, ..., 6$. Data in Tab. A.6 and Tab. A.7, respectively, in the appendix.

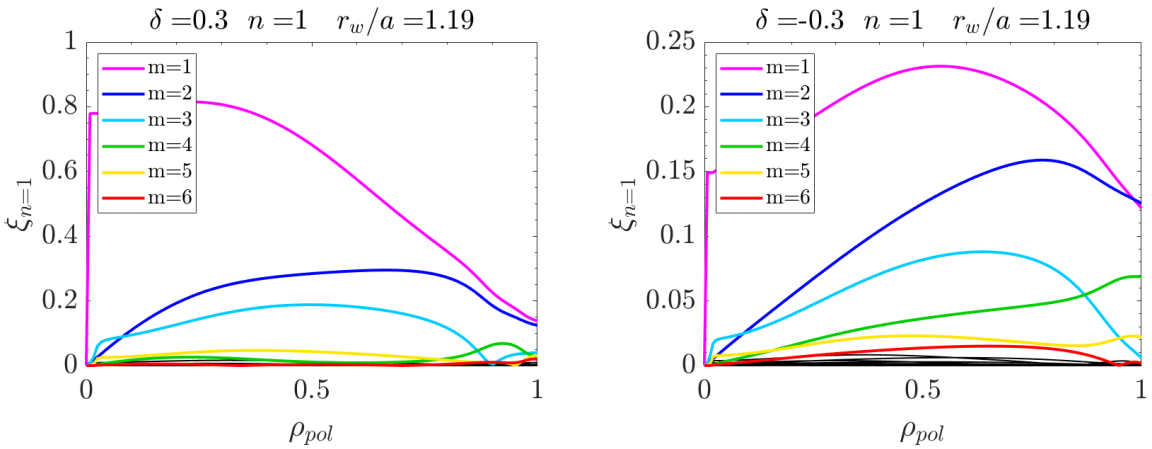

Figure 4.19: Eigenstate structure of the $n = 1$ mode for $\delta = 0.3$ and $\delta = -0.3$.

5 Summary and future work

In this thesis, the aim of this master thesis is to study the differences in plasma stability in the SMART tokamak when considering the presence or absence of the surrounding wall. Simulations over $n = 1, ..., 6$ have been carried out using the `CHEASE` and `MARS-F` codes.

The first objective of the work was to generate an equilibrium according to our objective, and simulate and evaluate the instabilities within it. The q-profile chosen was one in the advanced tokamak regime. The plasma shape with positive triangularity, $A = 1.97$, $B_0 = 0.37$ T and a total current $I_p < 500$ kA. It has been found that in our case, the most unstable modes are not the external kinks, but rather the infernal modes and the internal kink. This internal kink is driven by the high plasma pressure in the tokamak.

For the second part of the project, the goal was to include the ideal wall and study its effect on plasma stability. As seen in the literature, the wall has a significant influence over the growth rate the closer it is to the plasma surface. However, due to the presence of these internal kink and infernal modes, the full stabilization of the external kink at a certain wall radius via the computation of the growth rate could not be seen. Instead, it can be seen that the edge component of all modes disappears when the wall is close enough to the plasma. The plasma pressure limits found for the initial case: $\beta_{N,no-wall} \approx 2.4$ and $\beta_{N,ideal-wall} \approx 3.3$, which implies an increase of $\approx 37\%$ in the plasma pressure. To conclude this study, various AT regimes have been explored. It has been found that the plasma beta limit without the presence of a wall limit in SMART is $\beta_N = 3$, but it extends to as much as $\beta_N = 6$ when an ideal wall is introduced. This represents a significantly larger increase than anticipated, effectively doubling the beta value.

Lastly, a scan over positive and negative triangulatities has been conducted to give completeness to the work done. The current and pressure gradient profiles are fixed, and only the triangularity of the plasma has been changed. The result obtained is that positive triangularities have a better MHD stability than negative triangularities.These conclusions must be approached with caution as the plasma pressure varies substantially over the different triangularities, being the negative triangularities the ones with higher β_N, and plasmas at higher pressures are generally less stable. Nonetheless, positive triangularities has been found more stable than negative triangularities for low-n modes (the ones studied in this work) in other studies [41].

To continue this work, the resistivity of the wall should be included in the simulations. This would allow us to simulate a more real case and the RWM. The wall does not necessarily need to have the same shape as the plasma. The `CHEASE` code allows us to input an arbitrary shape for the wall. In this work, all positive values of m are considered until $m = 30$, but the presence of the $m = 1$ internal kink disturbs our analysis. The work can be repeated by excluding the $m = 1$, and thus the internal kink, for a more focused study of the wall effects on the external kink. Additionally, our simulations are based on the ideal MHD case, without considering resistivity, plasma rotation, and the effects of free particles. This would significantly change the results, as these mechanisms help control modes such as the infernal mode.

Acknowledgments

First of all I want to express my gratitude to Manolo and Eli, my supervisors, for the trust they placed in me to carry out this work and allow me to collaborate in this project. I've had a warm welcome to the PSFT group, and I hope I can continue working closely with you.

I want to give an special "thank you" to Jesús, for his invaluable assistance through this year. For teaching me how the codes work, the Matlab routines, helping me understand the MHD and infinite patience in reviewing all the complications I've had.

Finally, I would like to thank my family and friends, the true supports in my life, with whom I have shared countless moments and who have constantly motivated me to work hard towards achieving my goals.

A Data

Data tables from the growth rates computed.

Tag	$n=1$	$n=2$	$n=3$	$n=4$	$n=5$	$n=6$
ek6v4.0	3.34E-01	4.03E-01	4.27E-01	4.41E-01	4.49E-01	4.56E-01
ek6v3.8	3.18E-01	3.83E-01	4.05E-01	4.17E-01	4.25E-01	4.33E-01
ek6v3.6	3.02E-01	3.62E-01	3.81E-01	3.92E-01	4.01E-01	4.08E-01
ek6v3.4	2.84E-01	3.40E-01	3.56E-01	3.67E-01	3.76E-01	3.83E-01
ek6v3.2	2.65E-01	3.17E-01	3.30E-01	3.43E-01	3.50E-01	3.57E-01
ek6v3.0	2.45E-01	2.93E-01	3.04E-01	3.17E-01	3.22E-01	3.30E-01
ek6v2.8	2.23E-01	2.69E-01	2.78E-01	2.90E-01	2.95E-01	3.01E-01
ek6v2.6	2.00E-01	2.44E-01	2.51E-01	2.60E-01	2.68E-01	2.69E-01
ek6v2.4	1.76E-01	2.17E-01	2.24E-01	2.27E-01	2.41E-01	2.35E-01
ek6v2.2	1.51E-01	1.89E-01	1.98E-01	1.91E-01	2.13E-01	2.03E-01
ek6v2.0	1.24E-01	1.58E-01	1.74E-01	1.51E-01	1.80E-01	1.78E-01
ek6v1.8	9.58E-02	1.23E-01	1.51E-01	1.11E-01	1.39E-01	1.56E-01
ek6v1.6	6.57E-02	8.40E-02	1.27E-01	7.51E-02	8.50E-02	1.30E-01
ek6v1.4	3.08E-02	3.97E-02	9.95E-02	5.22E-02	2.32E-02	8.97E-02
ek6v1.2	5.24E-03	4.50E-03	6.77E-02	4.45E-02	4.21E-03	2.86E-02
ek6v1.0	2.40E-04	7.91E-04	2.98E-02	4.29E-02	2.77E-03	3.22E-03

Table A.1: Growth rates obtained with `MARS-F` code for the different pressures and modes $n = 1, ..., 6$ in the EK6 equilibrium.

$\mathbf{NV_M}$	r_w/a	$n=1$	$n=2$	$n=3$	$n=4$	$n=5$	$n=6$
80	1.99	2.27E-01	2.89E-01	3.03E-01	3.17E-01	3.22E-01	3.30E-01
72	1.89	2.21E-01	2.87E-01	3.02E-01	3.17E-01	3.22E-01	3.30E-01
64	1.79	2.14E-01	2.84E-01	3.01E-01	3.16E-01	3.22E-01	3.30E-01
56	1.69	2.04E-01	2.81E-01	3.00E-01	3.16E-01	3.22E-01	3.30E-01
48	1.59	1.92E-01	2.75E-01	2.97E-01	3.15E-01	3.21E-01	3.30E-01
40	1.49	1.76E-01	2.67E-01	2.93E-01	3.12E-01	3.20E-01	3.29E-01
32	1.39	1.57E-01	2.54E-01	2.85E-01	3.08E-01	3.18E-01	3.28E-01
24	1.29	1.35E-01	2.36E-01	2.71E-01	2.99E-01	3.12E-01	3.24E-01
16	1.19	1.13E-01	2.10E-01	2.47E-01	2.81E-01	2.98E-01	3.14E-01
8	1.09	9.12E-02	1.79E-01	2.11E-01	2.46E-01	2.66E-01	2.88E-01
1	1.00	7.15E-02	1.49E-01	1.67E-01	1.96E-01	2.10E-01	2.33E-01

Table A.2: Growth rates versus wall radius for $n = 1, ..., 6$ for the icw6v3.0 equilibrium.

	$n=1$		$n=2$	
β_N	no wall	$r_w/a=1$	no wall	$r_w/a=1$
6.087	4.459E-01	1.189E-01	5.625E-01	2.395E-01
6.015	4.355E-01	1.178E-01	5.469E-01	2.363E-01
5.939	4.245E-01	1.165E-01	5.310E-01	2.326E-01
5.859	4.128E-01	1.148E-01	5.148E-01	2.284E-01
5.775	4.008E-01	1.129E-01	4.981E-01	2.237E-01
5.686	3.883E-01	1.106E-01	4.807E-01	2.186E-01
5.592	3.754E-01	1.079E-01	4.622E-01	2.131E-01
5.493	3.621E-01	1.049E-01	4.429E-01	2.071E-01
5.388	3.481E-01	1.015E-01	4.230E-01	2.007E-01
5.276	3.335E-01	9.772E-02	4.029E-01	1.939E-01
5.157	3.181E-01	9.351E-02	3.824E-01	1.867E-01
5.031	3.016E-01	8.882E-02	3.614E-01	1.787E-01
4.895	2.840E-01	8.362E-02	3.396E-01	1.700E-01
4.750	2.651E-01	7.786E-02	3.167E-01	1.600E-01
4.594	2.447E-01	7.151E-02	2.930E-01	1.485E-01
4.426	2.230E-01	6.430E-02	2.686E-01	1.348E-01
4.246	2.001E-01	5.608E-02	2.436E-01	1.183E-01
4.051	1.759E-01	4.644E-02	2.173E-01	9.784E-02
3.840	1.505E-01	3.444E-02	1.891E-01	7.154E-02
3.612	1.238E-01	1.655E-02	1.579E-01	3.385E-02
3.364	9.567E-02	2.209E-03	1.231E-01	3.184E-04
3.096	6.564E-02	1.404E-03	8.393E-02	2.761E-04
2.805	3.072E-02	1.914E-04	3.959E-02	5.227E-04
2.489	5.234E-03	6.477E-04	4.492E-03	7.020E-04
2.146	1.794E-04	0.000E+00	7.980E-04	2.498E-04
c_2	5.54E-03	-8.72E-03	1.10E-02	-1.81E-02
c_1	7.60E-02	1.25E-01	5.74E-02	2.53E-01
c_0	-2.22E-01	-3.19E-01	-2.01E-01	-6.37E-01
R^2	0.99990	0.9993	0.9992	0.997

Table A.3: Computed growth rates for the $n=1$ and $n=2$ for the "no-wall" and $r_w/a=1$ cases. Below, the parameters of the second-grade polynomial fit. In red, the values not used to the fitting.

$M = 1.00,\ \mu = 0.7,\ A = 1.0$	$M = 1.00,\ \mu = 0.7,\ A = 2.5$
$M = 1.05,\ \mu = 0.7,\ A = 1.0$	$M = 1.05,\ \mu = 0.7,\ A = 2.5$
$M = 1.10,\ \mu = 0.7,\ A = 1.0$	$M = 1.10,\ \mu = 0.7,\ A = 2.5$
$M = 1.15,\ \mu = 0.7,\ A = 1.0$	$M = 1.15,\ \mu = 0.7,\ A = 2.5$
$M = 1.20,\ \mu = 0.7,\ A = 1.0$	$M = 1.20,\ \mu = 0.7,\ A = 2.5$
$M = 1.25,\ \mu = 0.7,\ A = 1.0$	$M = 1.25,\ \mu = 0.7,\ A = 2.5$
$M = 1.30,\ \mu = 0.7,\ A = 1.0$	$M = 1.30,\ \mu = 0.7,\ A = 2.5$
$M = 1.35,\ \mu = 0.7,\ A = 1.0$	$M = 1.35,\ \mu = 0.7,\ A = 2.5$
$M = 1.40,\ \mu = 0.7,\ A = 1.0$	$M = 1.40,\ \mu = 0.7,\ A = 2.5$
$M = 1.45,\ \mu = 0.7,\ A = 1.0$	$M = 1.45,\ \mu = 0.7,\ A = 2.5$
$M = 1.50,\ \mu = 0.7,\ A = 1.0$	$M = 1.50,\ \mu = 0.7,\ A = 2.5$
$M = 1.55,\ \mu = 0.7,\ A = 1.0$	$M = 1.55,\ \mu = 0.7,\ A = 2.5$
$M = 1.60,\ \mu = 0.7,\ A = 1.0$	$M = 1.60,\ \mu = 0.7,\ A = 2.5$
$M = 1.65,\ \mu = 0.7,\ A = 1.0$	$M = 1.65,\ \mu = 0.7,\ A = 2.5$
$M = 1.70,\ \mu = 0.7,\ A = 1.0$	$M = 1.70,\ \mu = 0.7,\ A = 2.5$
$M = 1.75,\ \mu = 0.7,\ A = 1.0$	$M = 1.75,\ \mu = 0.7,\ A = 2.5$
$M = 1.80,\ \mu = 0.7,\ A = 1.0$	$M = 1.80,\ \mu = 0.7,\ A = 2.5$
$M = 1.85,\ \mu = 0.7,\ A = 1.0$	$M = 1.85,\ \mu = 0.7,\ A = 2.5$
$M = 1.90,\ \mu = 0.7,\ A = 1.0$	$M = 1.90,\ \mu = 0.7,\ A = 2.5$
$M = 1.95,\ \mu = 0.7,\ A = 1.0$	$M = 1.95,\ \mu = 0.7,\ A = 2.5$
$M = 2.00,\ \mu = 0.7,\ A = 1.0$	$M = 2.00,\ \mu = 0.7,\ A = 2.5$
$M = 2.05,\ \mu = 0.7,\ A = 1.0$	$M = 2.05,\ \mu = 0.7,\ A = 2.5$
$M = 2.10,\ \mu = 0.7,\ A = 1.0$	$M = 2.10,\ \mu = 0.7,\ A = 2.5$
$M = 2.15,\ \mu = 0.7,\ A = 1.0$	$M = 2.15,\ \mu = 0.7,\ A = 2.5$
$M = 2.20,\ \mu = 0.7,\ A = 1.0$	$M = 2.20,\ \mu = 0.7,\ A = 2.5$
$M = 2.25,\ \mu = 0.7,\ A = 1.0$	$M = 2.25,\ \mu = 0.7,\ A = 2.5$
$M = 2.30,\ \mu = 0.7,\ A = 1.0$	$M = 2.30,\ \mu = 0.7,\ A = 2.5$
$M = 2.35,\ \mu = 0.7,\ A = 1.0$	$M = 2.35,\ \mu = 0.7,\ A = 2.5$
$M = 2.40,\ \mu = 0.7,\ A = 1.0$	$M = 2.40,\ \mu = 0.7,\ A = 2.5$
$M = 2.45,\ \mu = 0.7,\ A = 1.0$	$M = 2.45,\ \mu = 0.7,\ A = 2.5$
$M = 2.50,\ \mu = 0.7,\ A = 1.0$	$M = 2.50,\ \mu = 0.7,\ A = 2.5$
$M = 2.55,\ \mu = 0.7,\ A = 1.0$	$M = 2.55,\ \mu = 0.7,\ A = 2.5$
$M = 2.60,\ \mu = 0.7,\ A = 1.0$	$M = 2.60,\ \mu = 0.7,\ A = 2.5$
$M = 2.65,\ \mu = 0.7,\ A = 1.0$	$M = 2.65,\ \mu = 0.7,\ A = 2.5$
$M = 2.70,\ \mu = 0.7,\ A = 1.0$	$M = 2.70,\ \mu = 0.7,\ A = 2.5$
$M = 2.75,\ \mu = 0.7,\ A = 1.0$	$M = 2.75,\ \mu = 0.7,\ A = 2.5$
$M = 2.80,\ \mu = 0.7,\ A = 1.0$	$M = 2.80,\ \mu = 0.7,\ A = 2.5$
$M = 2.85,\ \mu = 0.7,\ A = 1.0$	$M = 2.85,\ \mu = 0.7,\ A = 2.5$
$M = 2.90,\ \mu = 0.7,\ A = 1.0$	$M = 2.90,\ \mu = 0.7,\ A = 2.5$
$M = 2.95,\ \mu = 0.7,\ A = 1.0$	$M = 2.95,\ \mu = 0.7,\ A = 2.5$
$M = 3.00,\ \mu = 0.7,\ A = 1.0$	$M = 3.00,\ \mu = 0.7,\ A = 2.5$

Table A.4: Parameters of the Gaussian distribution part of all surface averaged current profiles studied in the AT regime scan.

Triang.	$n=1$	$n=2$	$n=3$	$n=4$	$n=5$	$n=6$
$\delta=0.5$	2.45E-01	2.93E-01	3.04E-01	3.17E-01	3.22E-01	3.30E-01
$\delta=0.3$	2.58E-01	2.87E-01	2.92E-01	3.03E-01	3.05E-01	3.13E-01
$\delta=0.1$	3.57E-01	3.64E-01	3.72E-01	3.83E-01	3.90E-01	3.98E-01
$\delta=-0.1$	4.15E-01	4.15E-01	4.13E-01	4.15E-01	4.18E-01	4.24E-01
$\delta=-0.3$	5.05E-01	5.12E-01	5.22E-01	5.35E-01	5.48E-01	5.60E-01

Table A.5: Growth rates computed for the $n=1,...,6$ modes for different triangularities in the icw6v3.0 equilibrium. No wall is considered.

$\mathbf{NV_M}$	r_w/a	$n=1$	$n=2$	$n=3$	$n=4$	$n=5$	$n=6$
80	1.99	2.63E-01	3.13E-01	3.27E-01	3.41E-01	3.46E-01	3.55E-01
72	1.89	2.57E-01	3.11E-01	3.27E-01	3.41E-01	3.46E-01	3.55E-01
64	1.79	2.50E-01	3.09E-01	3.26E-01	3.41E-01	3.46E-01	3.54E-01
56	1.69	2.40E-01	3.06E-01	3.24E-01	3.40E-01	3.46E-01	3.54E-01
48	1.59	2.27E-01	3.01E-01	3.22E-01	3.39E-01	3.45E-01	3.54E-01
40	1.49	2.11E-01	2.93E-01	3.18E-01	3.37E-01	3.44E-01	3.54E-01
32	1.39	1.90E-01	2.81E-01	3.11E-01	3.33E-01	3.42E-01	3.53E-01
24	1.29	1.66E-01	2.63E-01	2.98E-01	3.25E-01	3.37E-01	3.50E-01
16	1.19	1.41E-01	2.39E-01	2.77E-01	3.09E-01	3.25E-01	3.41E-01
8	1.09	1.18E-01	2.10E-01	2.43E-01	2.78E-01	2.98E-01	3.19E-01
1	1	9.61E-02	1.78E-01	2.02E-01	2.32E-01	2.48E-01	2.71E-01

Table A.6: Growth rates computed versus wall radius for the $n=1,...,6$ modes for the icw6v3.0 equilibrium with $\delta=0.3$ triangularity.

$\mathbf{NV_M}$	r_w/a	$n=1$	$n=2$	$n=3$	$n=4$	$n=5$	$n=6$
80	1.99	4.75E-01	4.89E-01	4.97E-01	5.06E-01	5.14E-01	5.24E-01
72	1.89	4.70E-01	4.88E-01	4.97E-01	5.06E-01	5.14E-01	5.24E-01
64	1.79	4.65E-01	4.86E-01	4.96E-01	5.06E-01	5.14E-01	5.24E-01
56	1.69	4.57E-01	4.83E-01	4.95E-01	5.05E-01	5.14E-01	5.24E-01
48	1.59	4.47E-01	4.79E-01	4.94E-01	5.05E-01	5.14E-01	5.23E-01
40	1.49	4.34E-01	4.73E-01	4.91E-01	5.03E-01	5.13E-01	5.23E-01
32	1.39	4.15E-01	4.64E-01	4.85E-01	5.01E-01	5.12E-01	5.22E-01
24	1.29	3.87E-01	4.49E-01	4.76E-01	4.95E-01	5.08E-01	5.20E-01
16	1.19	3.45E-01	4.26E-01	4.60E-01	4.84E-01	5.01E-01	5.15E-01
8	1.09	2.81E-01	3.86E-01	4.29E-01	4.60E-01	4.81E-01	5.00E-01
1	1	1.76E-01	2.88E-01	3.45E-01	3.87E-01	4.19E-01	4.45E-01

Table A.7: Growth rates computed versus wall radius for the $n=1,...,6$ modes for the icw6v3.0 equilibrium with $\delta=-0.3$ triangularity.

B Acronyms and symbols

D	Deuterium
T	Tritium
He	Helium
n	Neutron
Li	Litium
AT	Advanced Tokamak (regime)
MHD	Magnetohydrodynamic
HFS	High Field Side
LFS	Low Field Side
RPPF	Pressure gradient input `CHEASE`
RFUN	Current density input `CHEASE`
LCFS	Last Closed Flux Surface
GR	Growth Rate
IK	Internal Kink
IF	Infernal mode
EK	External Kink
EIR	External-Internal Ratio
PT	Positive Triangularity
NT	Negative Triangulaity

Q	Fusion energy
n_α	α species number density
m_α	α species mass
$\mathbf{u}_\alpha$	α species velocity
p_α	α species pressure
ρ	Plasma density
$\mathbf{u}$	Plasma velocity
ρ_{el}	Charge density
$\mathbf{j}$	Current vector
p	Plasma pressure
$\mathbf{E}$	Electric field vector
$\mathbf{B}$	Magnetic field vector
∇	Gradient
$\nabla \cdot ()$	Spatial divergence
$\nabla \times ()$	Spatial curl
γ	Adiabatic coefficient
$\boldsymbol{\xi}$	Displacement vector
$\boldsymbol{F}$	Force
ω_n	Mode frequency
β	Plasma beta

β_N	Normalised plasma beta
j_ψ	Toroidal current density
ϕ	Toroidal angle
χ	Generalized poloidal angle
ψ	Poloidal magnetic flux
ψ_N	Normalized poloidal flux
ρ_{pol}	Radial flux coordinate
ω_A	Alfvén frequency
τ_A	Alfvén time
γ_0	Growth rate
$I_\parallel$	Surface averaged current
R_0	Major radius of magnetic axis
a	Plasma minor radius
A	Aspect ratio of the tokamak
B_0	Magnetic field at the magnetic axis
κ	Elongation
δ	Triangularity
I_p	Plasma total current
q	Safety factor
q_{min}	Minimum safety factor value
q_0	Safety factor at the core
q_{95}	Safety factor at 95% flux surface
q_{edge}	Safety factor at plasma edge
m	Poloidal mode number
n	Toroidal mode number
$a_w \equiv r_w$	Wall radius
r_c	Ideal wall critical radius
e	Electron charge, $1.602 \cdot 10^{-19}$ C
μ_0	Vacuum permeability, $1.257 \cdot 10^{-6}$ N·A^{-2}

References

[1] Raad H. Majeed and Osamah N. Oudah, 2018 J. Phys.: Conf. Ser. 1003 012076

[2] F. Wagner *et al*, Phys. Rev. Lett. 49, 1408 (1982)

[3] : R. J. Goldston *et al*, 1994 Plasma Phys. Control. Fusion 36 B213

[4] R. J. Buttery *et al*, Journal of Fusion Energy (2019) 38:72–111

[5] Yueqiang Liu, M.S. Chu, A.M. Garofalo, *et al.* Phys. Plasmas 13, 056120 (2006)

[6] Patrick J. Byrne, Study of External Kink Modes in Shaped HBT-EP Plasmas

[7] Yueqiang Liu, 2009 Plasma Phys. Control. Fusion 51 115006

[8] Physics of Plasmas (1994-present) 9, 3459 (2002)

[9] A.D. Turnbull *et al.* J. Plasma Phys. (2016), vol. 82, 515820301

[10] Y-K.M. Peng and D.J. Strickler, 1986 Nucl. Fusion 26 769 (1986)

[11] A. Sykes *et al*, 1992 Nucl. Fusion 32 694 (1992)

[12] Costley A.E. 2019 Towards a compact spherical tokamak fusion pilot plant. *Phil. Trans. R. Soc. A.* 377: 20170439. 20170439.

[13] S.J. Doyle, Fusion Engineering and Design, https://doi.org/10.1016/j.fusengdes.2021.112706

[14] A. Mancini *et al*, Fusion Engineering and Design, 171, 112542, (2021)

[15] J. Wesson. *Tokamaks*. Oxford University Press, 2004.

[16] V. Igochine, *Active Control of Magnetohydrodynamic Instabilities in Hot Plasmas*.

[17] H. Zohm, *Magnetohydrodynamic Stability of Tokamaks*

[18] R.J. Hosking and R.L. Dewar. *Fundamental Fluid Mechanics and Magnetohydrodynamics*. Springer, 2016.

[19] Lang L. Lao, Y.Q. Liu, Alan D. Turnbull, Encyclopedia of Nuclear Energy, 2021, Pages 431-458

[20] H. de Blank. *Theory of the m=1 kink mode in toroidal plasmas*

[21] Bussac MN *et al.*, (1975) Internal kink modes in toroidal plasmas with circular cross sections. Physical Review Letters 35: 1638.

[22] K. Kirby, 1988 Nucl. Fusion 28 231

[23] A Kleiner *et al.*, EUROFUSION WPS2-PR(16) 15726

[24] H.A. Holties *et al*, 1996 Nucl. Fusion 36 973

[25] G. Q. Dong, Y. Q. Liu, S. Wang, *et al*, Phys. Plasmas 24, 112510 (2017)

[26] M Okabayashi *et al*, 2002 Plasma Phys. Control. Fusion 44 B339

[27] S.C. Guo *et al*, 2016 Nucl. Fusion 56 056006

[28] Y. Q. Liu, *et al.*, Phys. Plasmas 7, 3681 (2000)

[29] MARS CODE MANUAL VOLUME I, KAERI/TR-2812/2004

[30] MARS CODE MANUAL VOLUME I, KAERI/TR-2811/2004

[31] H. Lütjens *et al*, ./Computer Physics Communications 97 (1996) 219-260

[32] Yueqiang Liu, Manual for running MARS-* series

[33] T. Ozeki *et al*, 1993 Nucl. Fusion 33 1025

[34] Yueqiang Liu *et al*, 2021 Nucl. Fusion 61 116022

[35] Rui HAN *et al*, 2020 Plasma Phys. Control. Fusion 62 085016

[36] Yueqiang Liu, Nucl. Fusion 55 (2015) 063022 (10pp)

[37] J. W. Berkery *et al*, 2020 Plasma Phys. Control. Fusion 62 085007

[38] J.E. Menard *et al*, 2003 Nucl. Fusion 43 330

[39] F. Troyon *et al*, 1988 Plasma Phys. Control. Fusion 30 1597

[40] Linjin Zheng *et al*, 2021 Nucl. Fusion 61 116014

[41] Zheng L.J., Koschenreuther M.T., Waelbroeck F.L. *et al*, 2018 Negative triangularity effects on tokamak MHD stability *IAEA-FEC,TH/P5-31*